

Contents lists available at ScienceDirect

Energy

journal homepage: www.elsevier.com/locate/energy



Tectonic evolution revealed by thermo-kinematic and its effect on shale gas preservation



Qianqian Feng ^{a, b}, Nansheng Qiu ^{a, b, *}, Tenger Borjigin ^c, Hang Wu ^{a, b}, Jiatang Zhang ^{a, b}, Baojian Shen ^c, Jiangshan Wang ^{a, b}

- ^a State Key Laboratory of Petroleum Resources and Prospecting, China University of Petroleum, Beijing, 102249, China
- ^b College of Geosciences, China University of Petroleum, Beijing, 102249, China
- ^c Wuxi Research Institute of Petroleum Geology, Sinopec Petroleum Exploration & Production Research Institute, Wuxi, 214126, China

ARTICLE INFO

Article history: Received 17 January 2021 Received in revised form 25 November 2021 Accepted 26 November 2021 Available online 30 November 2021

Keywords:
Tectonic evolution
Low-temperature thermochronology
Thermo-kinematic
Shale gas preservation

ABSTRACT

This study provides new insight for kinematic restoration in the thrust nappe and the effect of tectonic evolution on shale gas preservation was demonstrated in a case study from the Dingshan area in the southeastern Sichuan Basin, southwest China. The uplift process was reconstructed by sandbox experiment, discrete element method, vitrinite reflectance and thermochronology data, including apatite fission track, apatite (U–Th)/He and zircon (U–Th)/He. Thermo-kinematic analysis indicated that from southeast to northwest, the initial uplift time was getting earlier and the erosion increased, while the horizontal displacement decreased during the Alpine stage (Early Cretaceous-Eocene). During the Himalayan stage (Eocene-present time), it was characterized with rapid uplift as a whole. To study dynamic evaluation of shale gas preservation during tectonic evolution, the temperature and pressure evolution were revealed combining fluid inclusion analysis and basin modeling and variation in shale gas content was quantified. Differential uplift caused obvious differences in the process of cooling, pressure decreasing, fracturing and shale gas losing. With moderate uplift (~3350–3550 m), a few fractures generated in the shale and roof and few gas (~0.95–1.72 m³/t) diffused laterally. Enormous uplift (~5350 m) resulted in obvious fractures and massive gas loss (~3.22 m³/t) by lateral diffusion and vertical dissipation.

© 2021 Elsevier Ltd. All rights reserved.

1. Introduction

Shale gas is a kind of unconventional natural gas stored in shale formation. Compared with traditional fossil fuels, shale gas is more efficient and environmentally friendly [1]. It is an effective way to reduces a country's overdependence on high-pollution energy and help it to become carbon neutral [2]. With the severe energy shortage and high energy prices, shale gas has recently been a key onshore exploration target in many countries (Canada, Australia, Europe, China and other countries) [3]. The alleged revolutionary impact of shale gas on the long-run gas price levels is recommended by Caporin & Fontini [4] and Nick & Thoenes [5]. The U.S. Energy Information Administration (EIA) estimates that in 2019, U.S. shale gas production accounted for about 75% of total U.S.

natural gas production [6]. China is also known as one of countries that is relatively rich in shale gas resources and the Sichuan basin dominates the market [7]. By the end of 2020, more than 1 trillion cubic meters of shale gas reserves had been cumulatively proven in the Silurian Longmaxi Formation in the Sichuan Basin and the total production was more than $260 \times 10^8 \, \mathrm{m}^3$ (20 °C, 101 KPa) [8].

Shale reservoirs are complicated dual-porosity media system composed of a large number of pores and microfractures. These pore-fracture systems can further act as the storage spaces and main transport pathways of shale gas, and form hydrocarbon reservoirs [9,10]. The degree of natural fracture development in the shale reservoir with low-porosity and low-permeability is a controlling factor in gas producibility [11–13] and tectonic event is one of the main mechanisms causing fracture growth. In addition, the occurrence state of shale gas mainly includes the free state and the adsorption state depending on the formation pressure and temperature [14], which are also under the control of tectonic evolution. Therefore, the effect of tectonism on shale reservoirs is a core

^{*} Corresponding author. State Key Laboratory of Petroleum Resources and Prospecting, China University of Petroleum (Beijing), Beijing, 102249, China. E-mail address: qiunsh@cup.edu.cn (N. Qiu).

Nomencl	ature	U	the concentrations of 238U in the apatite or zircon grains, ppm
DSA	the Dingshan area	Th	the concentrations of 232Th in the apatite or zircon
DEM	the discrete element method		grains, ppm
Ro	Vitrinite reflectance	Ft	alpha correction factor
AFT	apatite fission track	eU	effect uranium concentration, ppm
AHe	apatite (U–Th)/He	Vb, V1-3	the detachment layers
ZHe	Zircon (U–Th)/He	Lb, L1-3	the rigid layers
QYF	the Qiyueshan Fault	d	thickness, cm
0	Ordovician	ρ	density, kg/m ³
S	Silurian	Kn	particle normal stiffness, N/m
D	Devonian	ks	particle shear stiffness, N/m
C	Carboniferous	bn	normal contact bond strength, N
P	Permian	bs	shear contact bond strength, N
T	Triassic	μ	coefficient of particle internal friction
J	Jurassic	η	viscosity, Pa•s
K	Cretaceous	GOF	goodness of fit
E-Q	Paleogene and Neogene	ACC	acceptable
ρs, ρi, ρd	the density of spontaneous, induce and dosimeter	MTL	mean track length, μm
	tracks, respectively, cm ⁻²	S	the shortening rate
Ns, Ni an	d Nd the number of spontaneous, induce and dosimeter tracks, respectively	T_p , T_0	the paleotemperature and paleo-surface temperature, °C
$P(\chi^2)$	the chi-square probability	G	the paleo-geothermal gradient, °C/km
SD	the standard deviation of measured confined track	Δh	the exhumation, m
	lengths, μm	Z_0	the present burial depth, m
N	the number of track lengths	P	the trapping pressure, MPa
Dpar	the long axis of track etch pit, μm	T	the trapping temperature, °C
t	(U–Th)/He ages, Ma	Th	the homogenization temperature, °C
⁴ He, ²³⁸ U	and ²³² Th the concentrations of ⁴ He, ²³⁸ U and ²³² Th in	a1, a2, a3,	, a4 the fit parameters of NaC1—H ₂ 0, KC1—H ₂ 0, CaC1 ₂
	the apatite or zircon grains, respectively		$-H_20$ and H_20 fluids, respectively;
$\lambda_{238}, \lambda_{235}$	and λ_{232} the decay constants	m	the molality, %

scientific issue within the petroleum industry and academia. The marine shale in the south China, is characterized by multi-stages of tectonic movement, and significant diversity in gas content and the preservation condition of shale gas in different evolution stages is one of the key projects to reveal the differential enrichment mechanisms of shale gas [15–19]. The preservation condition is controlled by several factors, such as the roof/floor conditions, the sealing properties of shale, faults, denudation and structural style, etc. Previous studies considered the sealing capacity of shale and roof/floor conditions are the basic factors determining whether the early formed hydrocarbons were preserved, while the intensity of tectonism, controlled the effusion, degree and abundance of shale gas, is the major controlling factor for shale gas preservation [16,18,20,21]. Uplift and denudation in the late tectonic stage could cause the pressure decreased and the diffusion coefficient of shale gas would increase [20,22,23]. The original balance would also be broken by the reduction of overburden pressure and the closed fracture would open again [13,20,24,25]. This is destructive to the preservation of shale gas. Actually, the major geological risk for the Mississippian Alum shale gas exploration activities in central Europe might be the loss of gas due to the major uplift of the area during Variscan Orogeny and the missing late gas generation [26]. Intensely folded and faulted, with gentle to steep layer dips and structural complexity is a major challenge to U.S. shale gas production, for example the Miocene Monterey shale [11], Middle Devonian Marcellus Shale [27,28] and the Eagle Ford shale [29].

The effect of tectonism on shale gas preservation has been analyzed qualitatively from the strength of fault, structural style, fractures and reformation time of uplift. A broad and gentle structure with continuous seal, moderate buried depth and

appropriate distance to fault zone is more favorable for the enrichment of shale gas [17,18,30,31]. It is highly probable that areas experiencing the greatest stress variation gradient would be most favorable to microfracture development. Triaxial tests on shales from North Sea reservoirs performed that uplift turned mudrocks into brittle overconsolidated materials [32]. Brittle shear resulted in percolating microfractures, which has a significant influence on the gas accumulation and enrichment of shale reservoirs [33,34]. The regional fractures of the Upper Triassic shale in the central China, the Lower Silurian shale in the South China, the Antrim Shale, Albany Shale and Lewis Shale in the North American continent are all considered to be related to uplift [12,13,18,35,36]. Exploration practices suggested that the late uplifting, small breaking distance and length of fault and weak fracture development are conducive to shale gas preservation [16,20,21,30,37,38]. In contrast, strongly deformed areas, where faults and high-angle large fractures were developed, are not conducive to the preservation of shale gas. Moreover, a preservation evaluation system combined with sealing conditions, the sealing properties of shale and tectonic effects (including the intensity and duration of late tectonic movements and the strength of fault) was also set up [21]. However, most of these studies are based on the qualitative analysis of static parameters. It is necessary to further study dynamic preservation and loss of shale gas during tectonic evolution. Furthermore, due to the fact that, at a regional scale, a few fractures would relax most of the tectonic loading and screen the development of pervasive microfracturing in the entire volume, direct evidence of the large-scale effect of tectonic forces on the development of microfractures at a regional scale remains to be found [39].

This study focused on the lower Paleozoic marine shale in the southeastern Sichuan basin to reconstruct the tectono-thermal evolution and explore the effect of tectonism on shale gas preservation. The Dingshan area (DSA) is one of the important shale gas area found in marine Silurian strata in the southeastern Sichuan Basin. As a thrust nappe structure controlled by Oiyueshan fault. **DSA** is characterized by significant differential northwest-southeast vertical uplift, horizontal zoning of pressure and gas content in the lower Silurian shale (Fig. 1). This area is favorable for a better understanding to the relationship between differential tectonothermal evolution and shale gas preservation. A variety of methods were integrated to reconstruct the Mesozoic-Cenozoic uplift history and characterize the change of shale gas content quantitatively during uplift processes in this study. First, the differential uplift process was constrained by new thermo-kinematic method composed of sandbox experiment, discrete element method (DEM), vitrinite reflectance (Ro) and low-temperature thermochronology data, including apatite fission track (AFT), apatite (U-Th)/He (AHe) and Zircon (U-Th)/He (ZHe). Then, the fluid inclusion analysis, basin modeling with Ro data were used to estimate the evolution of temperature and pressure. In addition, to study dynamic evaluation of shale gas preservation, we first reconstructed the 'burial-hydrocarbon generation-uplift-gas loss' evolution of shale, including the burial history, thermal history, hydrocarbon generation history, pressure evolution and shale gas content evolution. Finally, the influence of differential tectonothermal evolution on shale gas preservation is discussed. In this paper, new thermo-kinematic method combining sandbox experiment, discrete element method, vitrinite reflectance and lowtemperature thermochronology data was demonstrated for kinematic restoration in the thrust nappe with differential horizontal displacement. More importantly, our study provides new evidence for the large-scale effect of tectonic evolution on the development of fractures at a regional scale and dynamic analysis of shale gas preservation and loss during uplift process. The research result provides a scientific basis for the mechanism analysis of differential enrichment of shale gas and has an important significance for guiding the exploration of shale gas.

2. Geological setting

The Sichuan basin lies in the northwest of the Upper Yangtze Craton, southwest of China (Fig. 1a). The southeastern unit located between the Huayingshan Fault (HYF) and the Qiyueshan Fault (QYF) is a fold zone. It is tectonically bounded by the Hubei-Hunan-Guizhou Fold Belt in the southeast and the central uplift in the west, the eastern Sichuan Fold Belt in the north (Fig. 1b). The thin-skinned belt is well-developed with different structural styles. Separated by the QYF, it is varying from chevron anticlines and box synclines in the northwest to chevron synclines in the southeast (Fig. 1c). Both anticlines and synclines follow the thrust-fault distribution with stronger structural deformation. Located in the transitional zone of the Tethys-Himalayan tectonic domain and the Circum-Pacific tectonic domain, the southeastern Sichuan Basin has experienced multiple tectonic stages from Paleozoic to Cenozoic, including the Caledonian, Hercynian, Indosinian, Yanshanian (Alpine) and Himalayan movements (Fig. 1g). The structural deformation since the Early Cretaceous has established the present structural feature [40,41]. According to the characteristics of joints and faults, the structural form is mainly controlled by SE-NW compression in the Alpine stage (Early Cretaceous-Eocene) and approximately E-W compression in the Himalayan (Eocene-present time) [42–45]. The low-temperature thermochronology data indicated the southeastern Sichuan Basin experienced three tectonic evolution stags since Mesozoic [46-50],

including: (1) progressive tectonic deformation caused by north-westward convergence and collision between the Pacific plate and Eurasian plate during ~120-70 Ma; (2) slow uplift due to the tectonic inversion from the eastern China during ~70-40 Ma; (3) rapid uplift and denudation in response to the India-Asia collision after 40 Ma.

The southeastern Sichuan Basin fills with 8000–12000 m sediments deposited on the Precambrian basement (Fig. 1g), which consists of the marine sequence from the Paleozoic to Middle Triassic and the terrestrial sequence from the Late Triassic to Eocene [51,52]. Several giant shale gas fields were recently discovered in the lower Silurian Longmaxi Formation, such as Fuling, Weiyuan, Changning and Dingshan shale gas fields. By the end of 2019, the proven reserves of shale gas were 1790 \times 10 8 m 3 (20 °C, 101 KPa) [20]. According to the discovered shale gas fields, shale gas enrichment is closely related to tectonic evolution.

DSA is located Qiyueshan Fault zone near the eastern boundary of Sichuan basin with outcropped Triassic and Ordovician (Fig. 1f). As a thrust nappe structure controlled by QYF, the plane of **DSA** is shown as a northwest trending nose-shaped anticline. Five shale gas wells have been drilled in the area. The test production of well DY1, DY2 and DY5 are $3.4 \times 10^4 \text{ m}^3/\text{d}$, $10.5 \times 10^4 \text{ m}^3/\text{d}$ and $16.3 \times 10^4 \,\mathrm{m}^3/\mathrm{d}$ (20 °C, 101 KPa), respectively. Shale gas resources are abundant. There are significant differences with more than 2600 m in the depth of the lower Silurian Longmaxi Formation shale between the eastern and western (Fig. 1d), which indicated differential tectonic evolution in **DSA**. The high-quality shale with total organic carbon content (TOC) content ranging from 2.02% to 6.67% and Ro ranging from 2.03% to 2.28% is mainly developed at the bottom of the lower Silurian Longmaxi Formation [55]. The overlying caprock composed of the middle Silurian green silty mudstone and the upper section of the lower Silurian Longmaxi Formation and the underlying floor with the middle Ordovician dark gray limestone have good sealing. There are obvious differences in the gas content and pressure coefficient of the lower Silurian Longmaxi Formation shale, increased gradually from southeast to northwest (Fig. 1e). The mechanism of shale gas differential enrichment and preservation is still unclear.

The thermal paths constrained by the AFT indicate the Mesozoic-Cenozoic uplift process of **DSA** can be divided into three stages: (1) rapid uplift stage (~82-70 Ma), (2) slow uplift stage (~70-30 Ma) and (3) rapid uplift stage (~30 Ma-present time) [56]. It is necessary to further study the differential tectonic evolution. However, AFT can only reconstruct the thermal history of a rock sample through the partial annealing zone (PAZ) of ~60–125 °C [57–60], which is unable to accurately reveal the difference of uplift process. Therefore, thermo-chronometers with higher closure temperature are needed to study the differential uplift process.

3. Methods

3.1. Low-temperature thermochronology

The apatite He system is characterized by a PRZ in the range of ~40–75 °C [61] and the closure temperature of apatite crystals may vary based on differences in chemistry, parent nuclide zonation, size, and cooling rates [62,63]. Systematic diffusion studies indicated the zircon He PRZ of ~140–200 °C [64] and it has been demonstrated that high U–Th concentrations in zircon may impact helium diffusivity and attendant closure temperatures of individual grains, which may result in lower closure temperatures [65]. We can reconstruct the thermal history in the range of ~40–200 °C integrated AFT, AHe and ZHe. Three sandstone samples were collected from the central, northwestern and southeastern DSA. The detailed sample locations and lithology data are available in

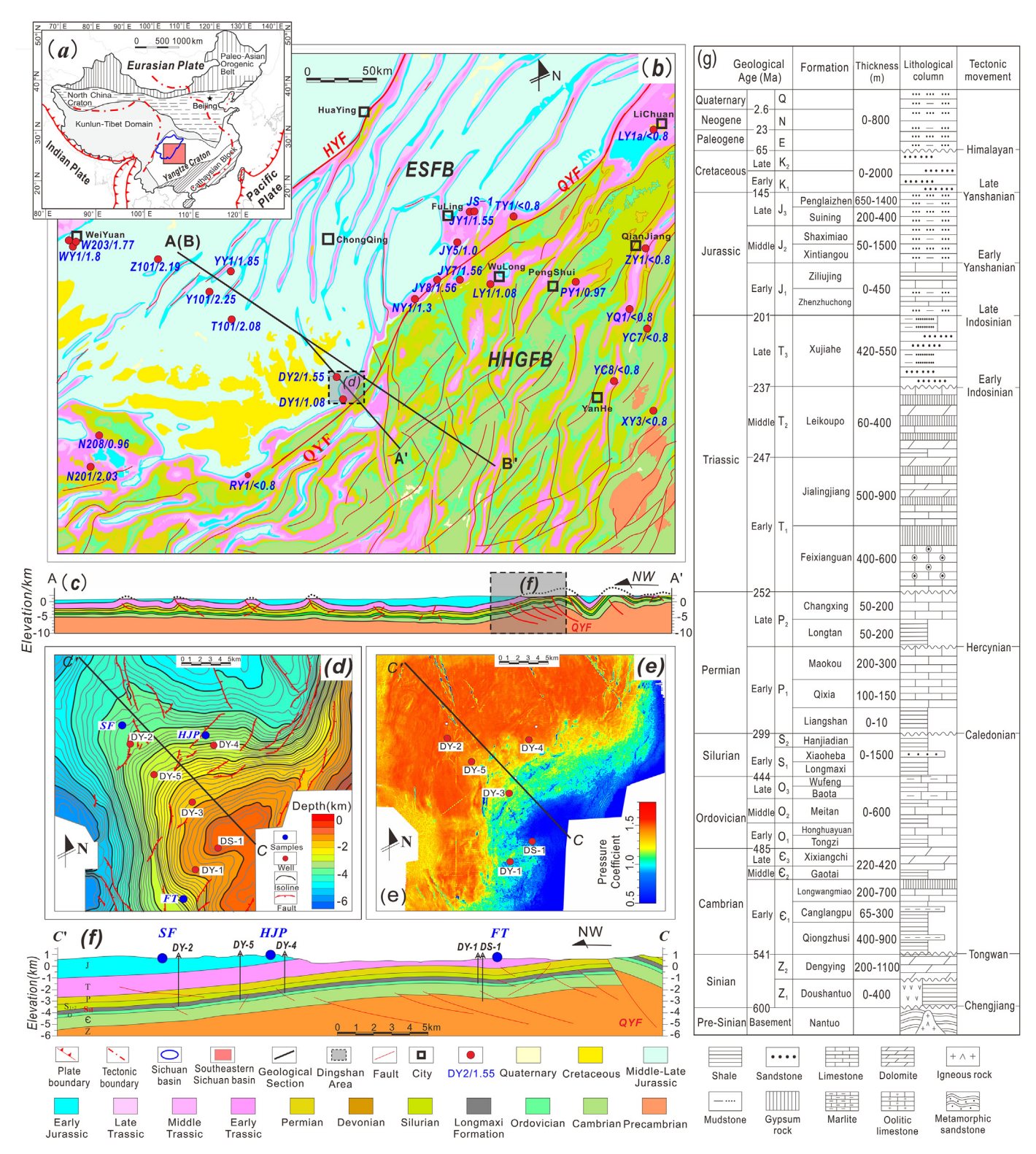


Fig. 1. (a) the tectonic location of the southeastern Sichuan Basin (modified after [53]); (b) Geological map of the southeastern Sichuan Basin. HYF-Huayingshan fault, QYF-Qiyueshan fault, HHGFB-the Hubei-Hunan-Guizhou Fold Belt, ESFB-the eastern Sichuan Fold Belt. (c) structural section of cross-section A-A', the plane location is shown in Fig. 1b; (d) Geological map of the lower Silurian in the Dingshan area (**DSA**); The blue points are the outcrop samples for low-temperature thermochronology analysis. (e) Pressure distribution map of the lower Silurian in **DSA**; DY2/1.55: the pressure coefficient of the lower Silurian Longmaxi Formation in the Well DY2 is 1.55. (f)Schematic diagram of cross-section C-C'. (g) Stratigraphic column and tectonic movements of the southeastern Sichuan Basin (modified after [54]). The Yanshanian movement is corresponding to the Alpine movement. The thin-skinned belt is well-developed with different structural styles in the Upper Yangtze. Separated by the QYF, it is varying from chevron anticlines and box synclines in the northwest to chevron synclines in the southeast. Five chevron anticlines and two box synclines developed in the cross-section B-B', which is the modeling profile of the sandbox experiment and discrete element numerical simulation. The pressure coefficient of shale is increased from southeast to northwest, while the pressure coefficient of shale in the basin is more than 2 and that outside the basin is generally less than 1. The characteristics of faults development indicates the intensity of late tectonic in the HHGFB is much stronger than that of the southeast Sichuan basin. The **DSA** is characterized by significant differential northwest-southeast vertical uplift, horizontal zoning of pressure in the lower Silurian shale. (For interpretation of the references to color in this figure legend, the reader is referred to the Web version of this article.)

Table 1, Fig. 1d and g.

AFT ages were determined using the external detector method at the Thermochronology Laboratory in China University of Petroleum, Beijing following the same procedures described by Chang et al. (2019) [66]. The AFT data is given in Table 2. The AFT central ages of samples, ranging from 61.1 \pm 4.5 Ma to 71.3 \pm 5.2 Ma, are significantly younger than their stratigraphic ages, which indicated these samples are likely to have remained in the AFT PRZ during the Late Cretaceous (Fig. 2a). The values of $P(\chi^2)$ are all greater than 5%, which shows that the age error is the statistical error. All grains come from the same source area and there are no foreign substances. The nonprojected mean track lengths of these samples ranged from 2.0 \pm 1.71 μm to 12.72 \pm 1.78 μm with the Dpar values between 2.04 μm and 2.56 μm .

The ZHe analyses were conducted at the School of Earth Science, University of Melbourne and AHe analyses were conducted at the Institute of Geology and Geophysics, Chinese Academy of Sciences. The (U—Th)/He thermochronology is a method in view of the He production via the nuclear decay of the U and Th in radioactive minerals. Based on the concentrations of ²³⁸U, ²³⁵U, ²³²Th and ⁴He in the apatite or zircon grains, we can obtain the (U—Th)/He ages (t) using the following equation:

$$^{4}He = 8 \times^{238}U(e^{\lambda_{238}t} - 1) + 7 \times \frac{^{238}U}{137.88}(e^{\lambda_{235}t} - 1) + 6 \times^{232}Th(e^{\lambda_{232}t} - 1)$$

$$(1)$$

where 4 He, 238 U and 232 Th is the concentrations of 4 He, 238 U, 235 U and 232 Th in the apatite or zircon grains, respectively. λ_{238} , λ_{235} and λ_{232} with values of 1.551×10^{-10} , 9.849×10^{-10} and 4.948×10^{-11} , are the decay constants [70]. For each sample, five apatite and zircon grains were tested and the AHe and ZHe data are given in Table 3 and Table 4.

Previous studies have suggested that the single grain AHe/ZHe ages are always characterized by obvious dispersion [62,72], which could be caused by various factors, including radiation damage [73,74], U–Th zoning [75], grain size [76], U- and/or Th-rich microinclusions [77], cooling rate [78], helium implantation from an external source [79], chemical influence [65], and grain breakage [80]. Shuster et al. (2006) suggested that the eU could be considered to be a proxy for the degree of radiation damage that resulted in the formation of traps that impede He diffusion [73]. The measured single grain AHe ages range from 12.11 \pm 0.67 Ma to 49.51 \pm 2.64 Ma. These ages are significantly younger than their

Table 1Details of the thermochronology samples in *DSA*.

Sample	Lithology	Stratigraphic Age (Ma)	Elevation (m)	Location
FT	Triassic sandstone	237–201	835	28°32′56.7″N; 106°38′20.55″E
HJP	Jurassic sandstone	174–163	657	28°41′22.03″N; 106°39′11.33″E
SF	Jurassic sandstone	174–163	837	28°42′23.62″N; 106°35′48.26″E

Table 2The measured AFT ages of the samples from the studied area.

Sample	Grain no.	ρs(10 ⁵ /cm ²) (Ns)	ρί(10 ⁵ /cm ²) (Ni)	ρd(10 ⁵ /cm ²) (Nd)	P(χ ²) (%)	Central age ±1σ(Ma)	Mean track length \pm SD(μ m) (N)	Dpar(μm)
FT	42	4.500 (504)	12.821 (1436)	16.460 (15118)	93.23	69.3 ± 5.2	12.0 ± 1.71 (41)	2.04
HJP	47	4.065 (449)	14.530 (1605)	16.337 (15118)	88.19	61.1 ± 4.5	$12.72 \pm 1.78 (58)$	2.12
SF	58	3.123 (626)	9.419 (1888)	16.584 (15118)	68.6	71.3 ± 5.2	$12.27 \pm 2.25 (53)$	2.56

 ρ s, ρ i and ρ d are density of spontaneous, induce and dosimeter tracks, respectively. Ns, Ni and Nd are number of spontaneous, induce and dosimeter tracks, respectively. P(χ 2) is chi-square probability [67]. Central AFT ages were calculated with Trackkey [68]. Ages were calculated using a $\zeta = 268.6 \pm 13.41$ for a standard IRMM540R glass. SD is the standard deviation of measured confined track lengths. N is the number of track lengths. Dpar is long axis of track etch pit, which is usually used as a proxy for the influence of chemical composition on track annealing [69].

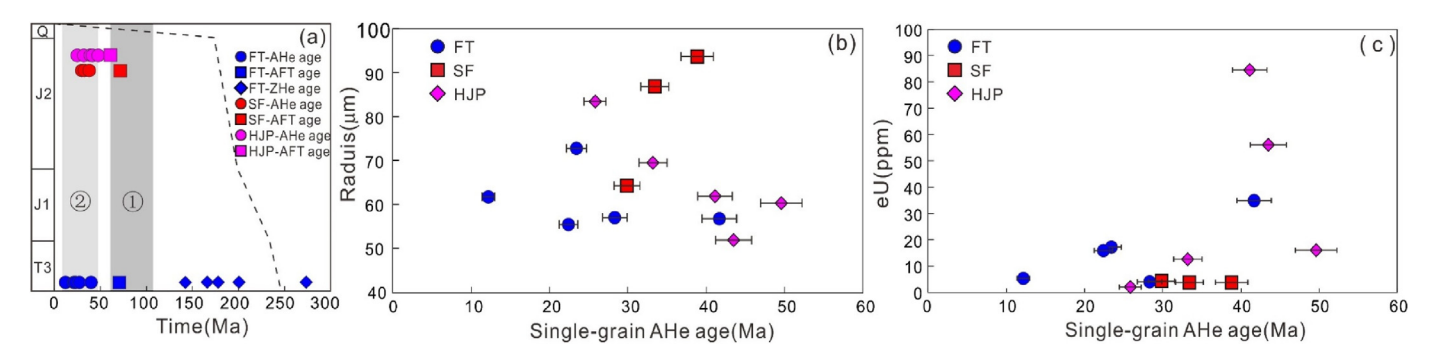


Fig. 2. (a)Relationship between the measured AFT, AHe and ZHe ages and the corresponding strata. The dashed line is the stratigraphic ages. The shadow area ① represents the Alpine exhumation event that occurred in DSA. The shadow area ② represents the exhumation event that occurred in Himalayan. (b) Correlation of single grain AHe age with radius. (c) Correlation of single grain AHe age with eU. The relationship between radius and single-grain AHe ages showed that there is no clear relationship between AHe age and grain size. The positive correlation between single-grain ages and eU indicates that the dispersion of single-grain AHe ages is probably due to radiation damage.

Table 3The measured AHe ages of the samples from the studied area.

Sample	Grain radius (µm)	⁴ He (nmol∎g ⁻¹)	Mass (μg)	FT	U (ppm)	Th (ppm)	eU (ppm)	Corrected age(Ma)	±1 σ (Ma)
Ft-A1	56.4	34.8	4.07	0.75	22.9	50.6	34.8	41.61	2.18
Ft-A2	55.3	15.7	4.37	0.74	8.3	31.6	15.7	22.34	1.18
Ft-A3	72.6	17.0	8.79	0.81	14.3	11.3	17.0	23.37	1.25
Ft-A4	61.4	5.2	6.18	0.75	0.0	22.0	5.2	12.11	0.67
Ft-A5	56.8	3.9	4.31	0.73	0.8	13.3	3.9	28.26	1.56
SF-A2	86.9	0.56	18.57	0.84	2.5	5.4	3.7	33.35	1.76
SF-A4	93.6	0.66	18.66	0.84	2.3	6.0	3.7	38.78	2.07
SF-A5	64.2	0.54	6.53	0.78	3.0	5.3	4.3	29.82	1.65
HJP-A1	61.7	14.53	5.90	0.78	73.0	50.1	84.7	41.07	2.19
HJP-A2	69.4	1.73	5.87	0.79	8.1	17.8	12.3	33.08	1.76
HJP-A3	83.4	0.24	13.64	0.81	0.5	7.1	2.1	25.74	1.39
HJP-A4	51.7	9.63	3.31	0.73	43.7	53.2	56.2	43.37	2.29
HJP-A5	60.1	3.26	5.35	0.76	9.9	26.0	16.0	49.51	2.64

Ft: alpha correction factor [71]. U: the concentrations of 238 U. Th: the concentrations of 232 Th. eU: effect uranium concentration, calculated from the contents of U and Th, eU = U+0.235Th [62].

Table 4The measured ZHe ages of the samples from the studied area.

Sample	Grain radius (µm)	⁴ He (nmol∎g ⁻¹)	Mass (μg)	FT	U (ppm)	Th (ppm)	eU (ppm)	Corrected age(Ma)	±1 σ (Ma)
Ft-Z1	61.3	47.02	9.94	0.79	202.7	125.0	232.0	165.2	10.2
Ft-Z2	66.1	22.89	10.13	0.81	108.4	90.0	129.5	141.8	8.8
Ft-Z3	54.9	20.10	6.13	0.77	116.2	68.9	132.4	200.0	12.4
Ft-Z4	52.2	55.28	4.27	0.74	346.3	145.0	380.4	273.1	16.9
Ft-Z5	74.7	84.13	13.46	0.83	253.1	135.6	285.0	177.6	11.0

depositional ages and represent apatite that has been completely reset. The relationship between radius and single-grain AHe ages showed that there is no clear relationship between AHe age and grain size (Fig. 2b). The positive correlation between single-grain ages and eU indicates that the dispersion of single-grain AHe ages is probably due to radiation damage (Fig. 2c). These samples gave uniform AHe ages, suggesting that they simultaneously experienced the AHe PRZ and recorded the rapid uplift during the Cenozoic (Fig. 2a). The single grain AHe ages from Triassic sample FT from the eastern DSA range from 12.11 to 41.61 Ma, which are younger than Jurassic samples HJP and SF, indicating that the eastern DSA experienced more recent exhumation. Sample FT gave five ZHe ages range from 141.77 \pm 8.79 Ma to 273.12 \pm 16.93 Ma, with four single-grain ZHe ages slightly younger than the stratigraphic ages and another was slightly older (Fig. 2a). The ZHe ages suggest the Triassic sample were only partially reset prior to cooling and retained thermal information from before the maximum depth was reached, which indicated the maximum paleotemperature of the Triassic strata just entered the PRZ of zircon and cannot represent the last uplift time.

3.2. Sandbox experiment

In this study, one set of sandbox experiments was carried out in China University of Petroleum, Beijing to reproduce the deformation and shortening process of B–B' profile since the Alpine stage. The data based on balanced restoration indicated that the total shortening of the eastern Sichuan fold belt is ~140 km (~24% shortening) [50,81] and a shortening rate of 1–2 mm/yr [54,81]. Therefore, we set the shortening ratio of the B–B' profile as 25% and the original length was approximately ~480 km before shortening. According to thermochronology data (Fig. 3), the D-D' profile has experienced a significant progressive deformation with a 'rapid-slow-rapid' cooling process: (1) rapid uplift stage (~180-70 Ma), (2) slow uplift stage (~70-40 Ma) and (3) rapid uplift stage (~40 Ma-present time). Furthermore, Northrup et al. (1995) and Li et al. (2014) suggested the rate of Pacific-Eurasia convergence declined

from ~120 to 140 mm/yr in the Late Cretaceous to ~30-40 mm/yr in the Eocene [44,82]. Then we can define the tectonic evolution of the B–B' profile can be divided into three major stages: (1) rapid uplift stage (~140-70 Ma), (2) slow uplift stage (~70-40 Ma) and (3) rapid uplift stage (~40 Ma-present time). Noted that the effect extent of compression stress in the southeast direction during the Himalayan are still controversial. Therefore, we only simulate the tectonic evolution under SE-NW compression from the Late Cretaceous to the Oligocene (~140-40 Ma). The sandbox experiments were carried out in a 120 cm \times 20 cm Plexiglas box filling with brittle and ductile materials (Fig. 4). The length ratio of model/nature is 2.5×10^{-6} . The gravity (g), density (ρ) and viscosity (η) ratio of model/nature are 1, 1 and $2 \times 10^{-17} - 1 \times 10^{-16}$, respectively. The time ratio is about $8 \times 10^{-12} - 4 \times 10^{-11}$, i.e., 1 h in model represents the geological time of 2.8–14.2 Ma, which means that an extrusion rate of 0.84-4.26 cm/h would be appropriate when the stratum is shortened by 120 km within 100 Ma. In this study, the sandbox experiment with variable rate was carried out: 1.8 cm/h from the Early Cretaceous to the Late Cretaceous (~140-70 Ma) and 0.9 cm/h from the Late Cretaceous to the Oligocene (~70-40 Ma).

Multilayer detachment folding is the dominant way of deformation in the southeastern Sichuan Basin [40,50,54]. There are four main regional detachment layers developed in the southeastern Sichuan basin: (1) the basement decollement horizon with the depth of 14-16 km and the thickness of deformed basement is 3–4 km [83,84]; (2) the Middle-Lower Cambrian shale and gypsum with a thickness of 500-1000 m, (3) the Silurian shale with the average thickness of 1500 m and (4) the Triassic gypsum and salt with a thickness of 1000 m [50]. The seismic profile shows that the QYF is a reverse fault cutting deeply into the basement with dip angles of 30-40° [85]. Zhang et al. (2015) speculated that the QYF experienced inheriting activity and its shallow part pushed northwestward and then become gently inclined since the Late Jurassic [86]. For better reproducing the uplift process, we forced to set the pre-existing fault QYF and four detachment layers before modeling. However, the sand content of the Silurian strata in the wide spaced anticlines increases significantly [87], which leads to a

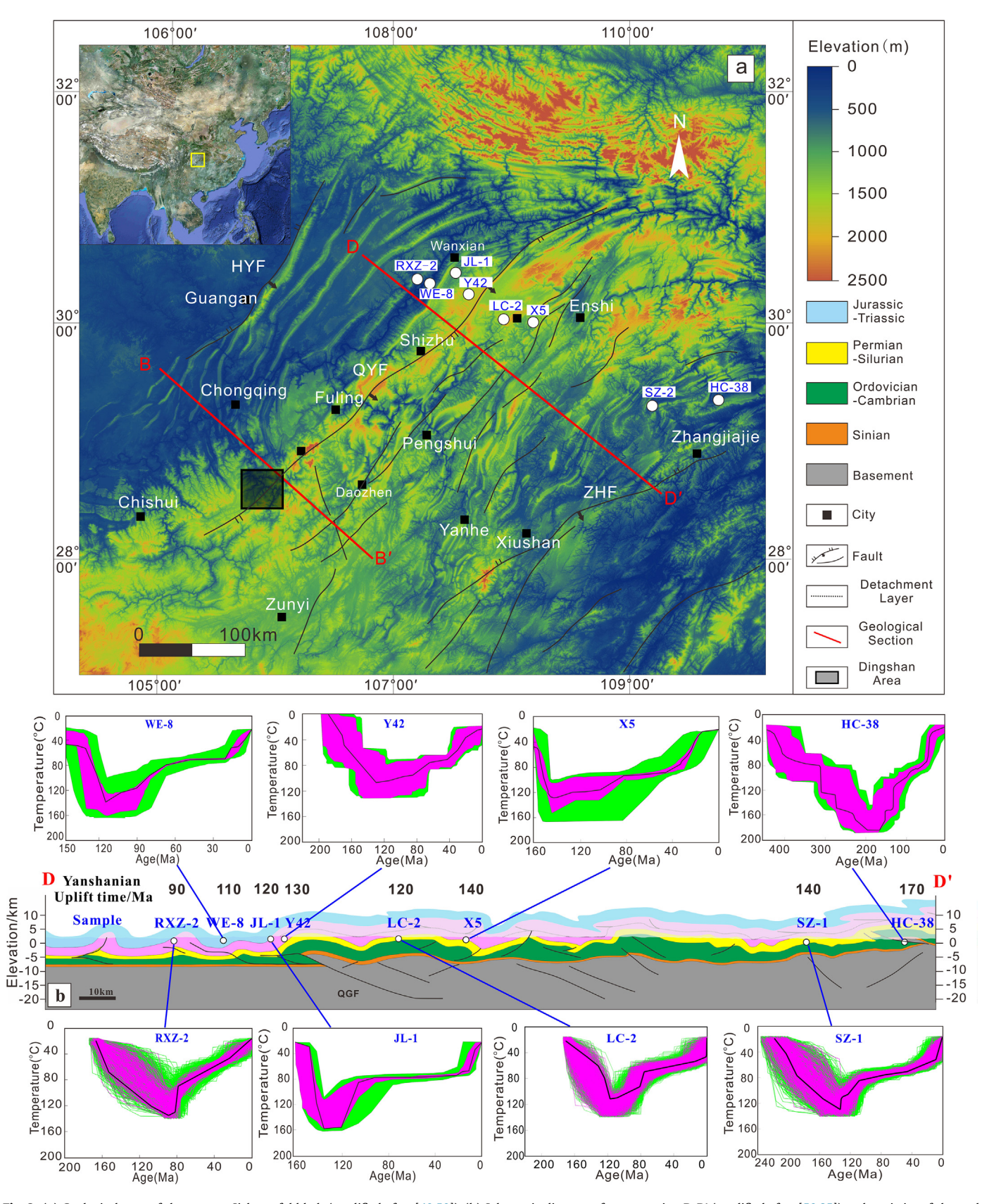


Fig. 3. (a) Geological map of the eastern Sichuan fold belt (modified after [40,50]). (b) Schematic diagram of cross-section D-D' (modified after [50,85]) and statistics of thermal history in the eastern Sichuan fold belt. RXZ-2, LC-2, SZ-1: [50]; HC-38 [91]: ; WE-8, JL-1, X5: [47]; Y42: [92]. According to thermochronology data, the D-D' profile has experienced a significant progressive deformation with a 'rapid-slow-rapid' cooling process: (1) rapid uplift stage (~180-70 Ma), (2) slow uplift stage (~70-40 Ma) and (3) rapid uplift stage (~40 Ma-present time). B-B' is the modeling profile, shown as Fig. 1b.

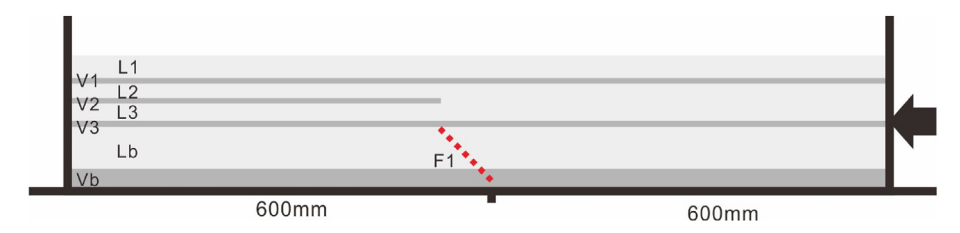


Fig. 4. The model setup of sandbox and numerical experiment. The detachment layers were named as Vb and V1-3 and the rigid layers were named as Lb and L1-3. F1 represents OYF with dip angles of 40°.

weakness of detachment effect and most of them are involved in deformation. Therefore, the detachment of Silurian was only set up for wide spaced synclines. For the model, the silicone polymers with a viscosity of 9×10^3 Pa•s and a density of 0.95 g/cm³ was used to simulate the detachment layers. The silicone polymer shows Newtonian behavior at a low strain rate [88]. We used glass microbeads with a density of 2600 kg/m³ and a grain size of 180-250 µm to simulate the rigid layers. Glass micro-beads have almost no cohesion and an internal friction angle of about 25° , and their mechanical properties lie between dry quartz sand and silicone resin and therefore are suitable for simulating folding [89,90]. All model parameters are shown in Table 5.

3.3. Discrete element method (DEM)

The discrete element method (DEM) can simulate granular material by using distinct rigid particles. In this study, the twodimensional Particle Flow Code (PFC2D), developed by the Itasca Consulting Group was applied to carry out discrete element numerical experiments. PFC2D simulates the mechanical behavior of a system which consists of a collection of particles with different sizes. The physical parameters of particles should be defined, such as density, contact stiffness, friction, viscosity, etc. The mechanical behavior is described by the movement of each particle and the force and moment acting at each contact. All contact forces, including normal and shear force acting on a single particle are calculated together following the Newton's law to determine the particle displacements. It is worth noting that this method can record the kinematic paths of discrete elements. The numerical experiments with the same geometry (Fig. 4) and extrusion rate as the sandbox model were carried out to characterize the deformation process of B–B′ profile since the Alpine stage. The microscopic mechanical properties of the particles are shown in Table 5. In the model, circular particles distributed evenly were used to simulate the interlayer detachment layers (V1-3) and the rigid layers and basement detachment layer (Vb) were composed of circular particles distributed randomly. The pre-existing QYF was simulated by generating the wall with a friction coefficient of 0. The model was composed of 6285 circular particles with a porosity of 20%. During the simulation process, we extracted the displacement parameter of the particles with a view to clear the horizontal and vertical displacement characteristics of the model system. Furthermore, we selected 20 particles throughout the Qiyueshan area after the PFC simulation and extracted their displacement parameters, which was used to discuss the structural deformation process of the study area.

4. Results

4.1. Thermal modeling

HeFTy software with the Monte Carlo approach was used to invert the thermal histories. Different models were selected for each indicator, specifically, the multikinetic annealing model [59] proposed by Ketcham et al. (2007) for AFT, the zircon and apatite radiation damage accumulation and annealing models [65,74] developed by Guenthner et al. (2013) and Flowers et al. (2009) for ZHe and AHe. In our modeling, some geological constraints, including the time range, temperature range, and present-day surface temperature, were added to obtain a more reliable thermal history path in the simulation. Previous studies stated that the Qiyueshan area began to undergo exhumation of the Alpine stage at 125-82 Ma, while the rapid uplift of the Himalayan occurred at 40-20 Ma [46,47,50,56,93] based on AFT ages. Therefore, the constrained time ranges were set to 125-80 Ma and 40-20 Ma. In addition, the prior temperature range was set to 20-200 °C to capture the range of temperature sensitivities expected for ZHe, AFT and AHe. The present-day surface temperature was set to 15 ± 15 °C. In our modeling, 30000–50000 thermal paths were developed and we set the range of temperature and time sensitivities as new constraints, which were shown in Fig. 5. Then new thermal history was modeled and the best-fit time-temperature path indicated the thermal history of the sample. The sample FT was modeled by integrating the ZHe, AHe and AFT data (Fig. 5a). The thermal modeling results showed that the first cooling occurred during the early Late Cretaceous (105-80 Ma) and caused the sample to cool from ~165 °C to ~70 °C at a cooling rate of ~3.8 °C/Ma. The thermal histories of samples HJP and SF were

Table 5Experiment parameters of sandbox and numerical experiment.

Layer	Stratum	d(cm)	$\rho (kg/m^3)$	kn(N/m)	ks (N/m)	bn bs(N)	μ	η(Pa•s)
L1	T ₂ -K	0.7	2600	3 × 10 ⁹	1 × 10 ⁹		0.7	
V1	T ₁	0.2	1000	1.5×10^7	0.5×10^{7}	8×10^4	0.2	1×10^4
L2	S ₂ -P	0.4	2600	3×10^9	1×10^9		0.7	
V2	S ₁	0.3	1000	1.5×10^{7}	0.5×10^{7}	8×10^4	0.2	1×10^4
L3	€2-3-0	0.4	2600	3×10^9	1×10^9		0.7	
V3	$\epsilon_{\scriptscriptstyle 1}$	0.2	1000	1.5×10^{7}	0.5×10^{7}	8×10^4	0.2	1×10^4
Lb	Base-Z	2.0	2600	3×10^9	1×10^9		0.7	
Vb	Base	0.8	1000	1.5×10^{7}	0.5×10^{7}	8×10^4	0.2	1×10^4

d-thickness, ρ -density, kn-particle normal stiffness, ks-particle shear stiffness, bn-normal contact bond strength, bs-shear contact bond strength, μ -coefficient of particle internal friction, η -viscosity.

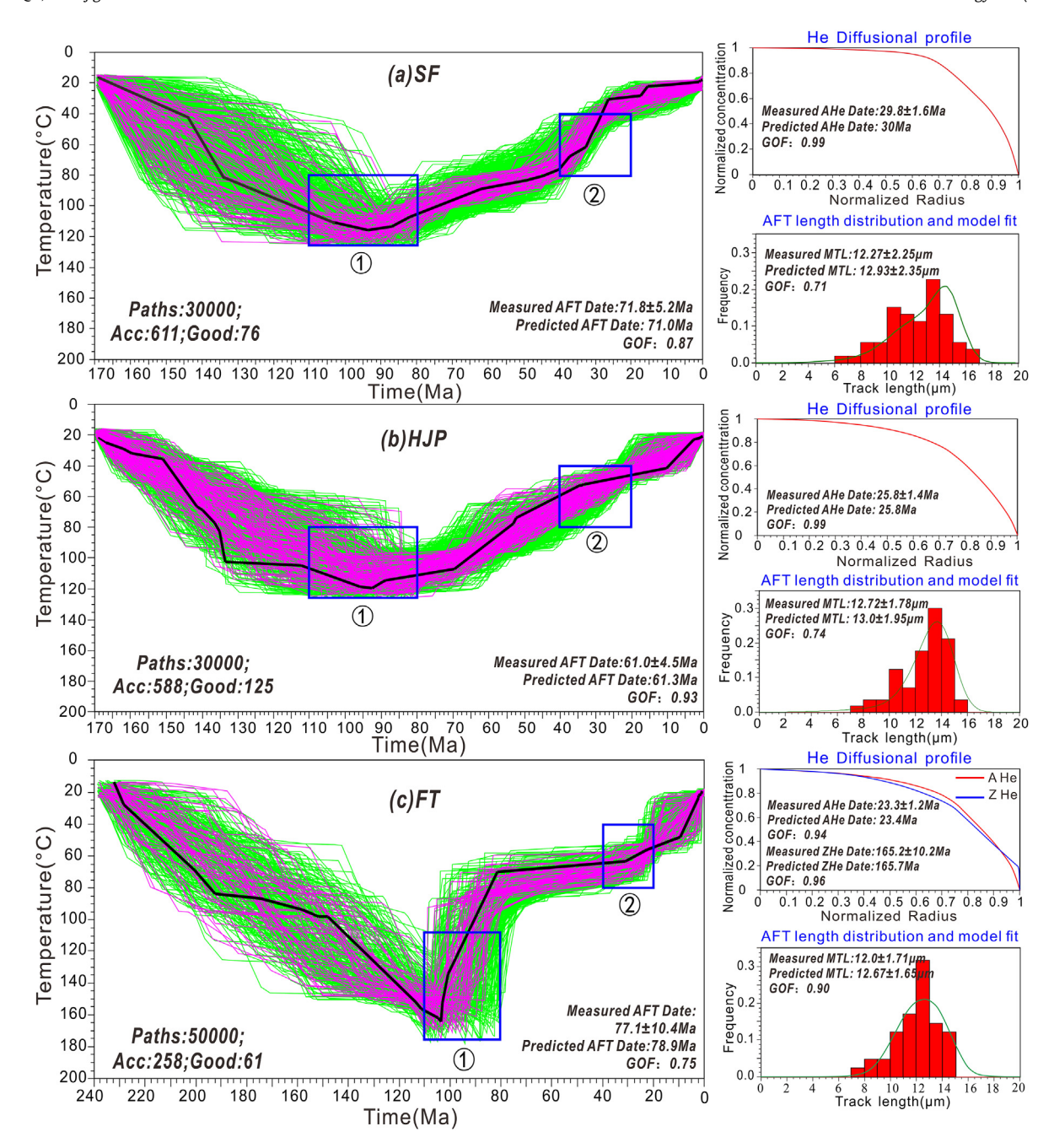


Fig. 5. Thermal inversion results reconstructed by AFT, AHe and ZHe. Green lines = acceptable fit paths (GOF >0.05), Magenta lines = good fit paths (GOF >0.5), Black lines represent the best time-temperature paths. GOF = goodness of fit. ACC = acceptable. MTL = mean track length. The blue box⊚represents constraints for the Alpine exhumation event. The blue box⊚represents constraints for the exhumation event that occurred in Himalayan. The sample FT experienced the first cooling stage at 105 Ma, while the Sample HJP and SF began to cool rapidly at ~95 Ma. The initial time of the Alpine rapid uplift was getting later from southeast to northwest in DSA. (For interpretation of the references to color in this figure legend, the reader is referred to the Web version of this article.)

obtained by their AHe and AFT data (Fig. 5b and c). The modeling results showed the samples began to cool rapidly at ~95 Ma. Note that the thermal histories of three samples indicated that the initial time of rapid uplift during the early Late Cretaceous was getting later from southeast to northwest.

4.2. Sandbox experiment

The sandbox experiment results were shown as Fig. 6, Supplemental Material S1a. Under compressional stress from the left, the deformation first occurred in the left part of the sandbox (Fig. 6).

The basal detachment involved deformation, thus resulted in two box anticlines in sequence (Fig. 6a and b). When the shortening ratio was 9%, the pre-existing QYF became active (F10 shown in Fig. 6c). The continuous compression led to overthrust of the basement onto a higher level and formed a thrust nappe due to QYF (Fig. 6d). Meanwhile, obvious differential horizontal displacement occurred to the upper layers. The area where deformation first occurred has more horizontal displacement, which indicated that the deformation first occurred in the northwest part away from the extrusion end in the Qiyueshan area. The QYF connected the deep basement decollement horizon and the shallow detachment layers,

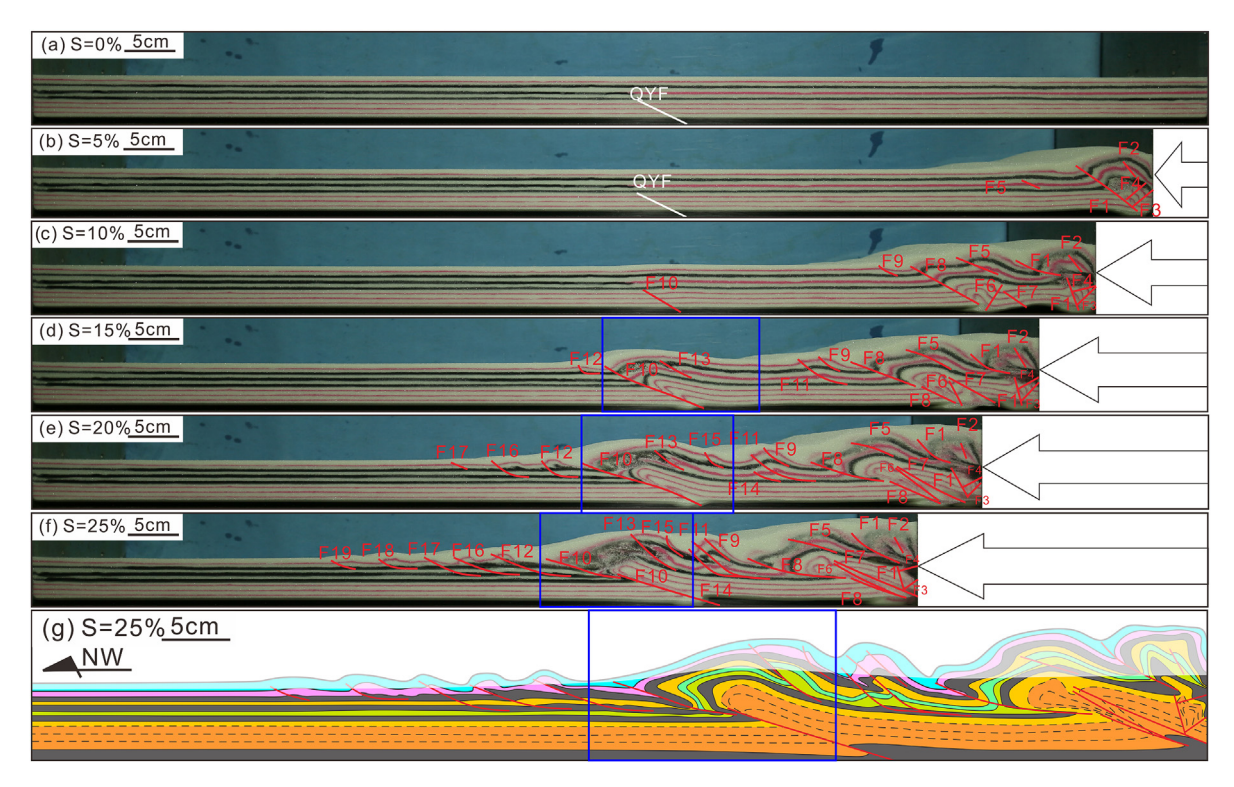


Fig. 6. (a)—(f) sandbox experiment results. (g) the interpreted of the tectonic pattern after 25% of shortening (f) based on geological scale and the eroded part was displayed in light color. F1-19: thrust faults numbered in the order of their formation. S: the shortening ratio of the model. The blue box represents the Qiyueshan anticline. Five chevron anticlines occurred to the northwest, the Qiyueshan anticline in the middle and two box anticlines to the southeast at 25% of shortening. The Qiyueshan anticline began to form when the shortening ratio was 9%, and the initial time of the Alpine uplift event was getting later from northwest to southeast. (For interpretation of the references to color in this figure legend, the reader is referred to the Web version of this article.)

including Silurian shale and the Triassic gypsum. Further shorting caused the shallow detachment layers involved deformation. Some chevron anticlines formed in the northwest with simultaneous development of shallower detachment faults, whereas the Middle-Lower Cambrian shale and gypsum rock was developed forward and another anticline occurred to the southeast (Fig. 6e). Finally, five chevron anticlines occurred to the northwest, the Oiyueshan anticline in the middle and two box anticlines to the southeast (Fig. 6e and f). The model morphology at 25% of shortening (Fig. 6f) is very similar to structural style of section B-B' (Fig. 1b and c), including tectonic zoning, the number of chevron anticlines and box anticlines and even stratigraphic outcrops. Therefore, we believe that this result of the model can be regarded as the deformation of section B–B′ caused by SE-NW compression in the Alpine stage (~140-40 Ma) and the Qiyueshan anticline can be regarded as **DSA**. We can determine the geological time at a certain shortening rate (S, %) using the following equation:

$$t = \begin{cases} 140 - S \times \frac{T_1}{S_1}, \ 0 \le S \le 20.6\% \\ \\ 70 - \left(S - 0.206\right) \times \frac{T_2}{S_2}, \ 20.6\% \le S \le 25\% \end{cases} \tag{2}$$

where $T_1 = 70$ Ma, the time region (~140-70 Ma) of simulation with an extrusion rate of 1.8 cm/h; S_1 , the shortening rate with an extrusion rate of 1.8 cm/h, $S_1 = 25\% \times \frac{14}{17} \approx 20.6\%$; $T_2 = 30$ Ma, the time region (~70-40 Ma) of simulation with an extrusion rate of 0.9 cm/h; S_2 , the shortening rate with an extrusion rate of 0.9 cm/h, $S_2 = 25\% \times \frac{3}{17} \approx 4.4\%$. According to the modeling results, the Qiyueshan anticline began to form when the shortening ratio was 9%, which indicated **DSA** began to uplift at ~110 Ma and the initial

time of the Alpine uplift event was getting later from northwest to southeast.

4.3. Discrete element numerical modeling

The discrete element numerical modeling results, shown as Fig. 7, Supplemental Material S1b-c, are generally consistent with sandbox experiment results (Fig. 6). There are two box anticlines formed in sequence at the southeast of the QYF (Fig. 7b). When the shortening ratio was 9%, the pre-existing QYF became active (Fig. 7c). After 20% of shortening, chevron anticlines began to generate at the northwest of the QYF (Fig. 7e and f). The displacement results of particles shown that differential uplift occurred to the Qiyueshan area (Fig. 7h). The horizontal displacement decreased from southeast to northwest (Figs. 7h-1, Supplemental Material S1b), while the vertical displacement increased (Figs. 7h-2, Supplemental Material S1c). These indicated the particles first uplifted with more horizontal displacement moved to the northwest of the Qiyueshan anticline and the particles uplifted later with less horizontal displacement remained in the southeast. Finally, the initial time was getting later from northwest to southeast. The geological time at a certain shortening rate (S, %) was also calculated using equation (1). We noted that only three chevron anticlines formed with the weak deformational extent when modeling ran for a long time and the Qiyueshan anticline has higher amplitude. This is mainly because the larger particles in PFC2D were more difficult to horizontal move and shallow detachment layers involved deformation weakly.

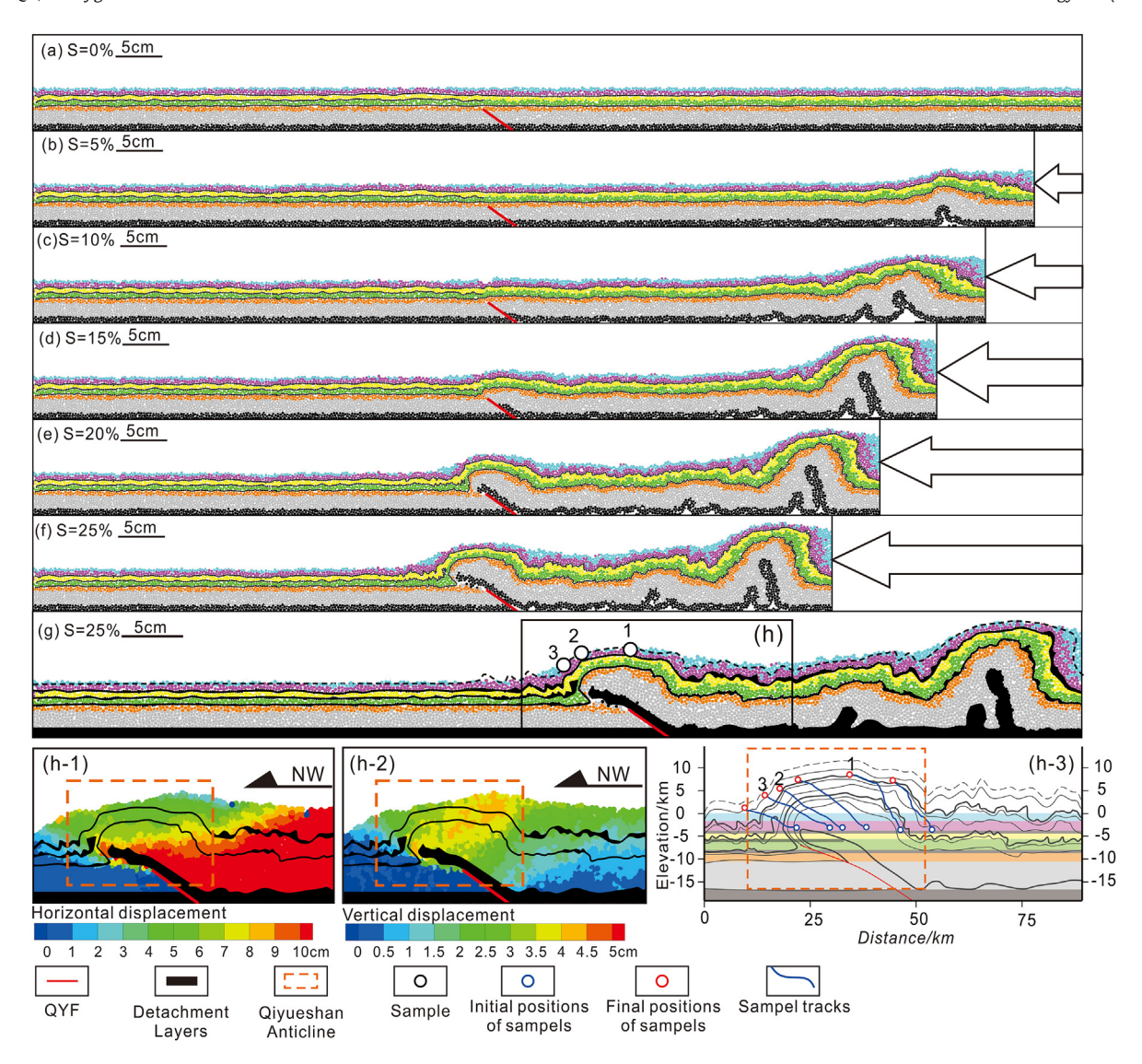


Fig. 7. (a)—(f) Discrete element numerical results. S: the shortening ratio of the model. (g) the interpreted of the tectonic pattern after 25% of shortening. The white circles numbered 1–3 in h are constraint particles that match sample Ft, HJP and SF, respectively. (h-1) Horizontal displacement fields of the Qiyueshan anticline. (h-2) Vertical displacement fields of the Qiyueshan anticline. (h-3) Sample tracks after 25% of shortening. The black lines show the model configuration. When the shortening ratio was 9%, the pre-existing QYF became active. In the Qiyueshan area, the horizontal displacement decreased from southeast to northwest, while the vertical displacement increased. These indicated the particles first uplifted with more horizontal displacement moved to the northwest of the Qiyueshan anticline and the particles uplifted later with less horizontal displacement remained in the southeast. The initial time of the Alpine uplift event was getting later from northwest to southeast.

5. Thermo-kinematic analysis

The kinematic molding results of the Alpine uplift event in **DSA** (Figs. 6 and 7) are contrary to the thermal histories (Fig. 5). The thermal histories showed the samples began to cool rapidly at ~95 Ma and the initial time of rapid uplift of the Alpine uplift event was getting later from southeast to northwest. The kinematic molding results showed that the Qiyueshan anticline began to form when the shortening ratio was 9%, which indicated **DSA** began to uplift at ~110 Ma and the initial time of the Alpine uplift event was getting later from northwest to southeast. In order to get more accurate uplift process and exhumation, some kinematic constraints based on sandbox experiments and numerical simulations were given in the thermal modeling. We set the constrained time ranges of Alpine exhumation as 105 ± 5 Ma for sample FT, 110 \pm 5 Ma for sample HJP and 110 \pm 5 Ma for sample FT. The constrained time ranges of the Himalayan exhumation were set as 40 ± 5 Ma for three samples. The present-day surface temperature was set as 15 \pm 15 °C and the prior temperature range was set as 20–200 °C to capture the range of temperature sensitivities. Three particles were also collected at the corresponding structural position and the recorded paths were constrained by retaining the movement tendency (Figs. 7h–3) and revising the amount of uplift based on sandbox experiment (Fig. 6g). Then we converted recorded kinematic paths of samples into the temperature paths to constrain thermal histories.

Fig. 8 shows the thermo-kinematic results. The best-fit time-temperature paths represent the thermal history of samples. The sample SF, from the northwestern of *DSA*, cooled rapidly during 110–60 Ma and the temperature decreased from ~120 °C to ~85 °C at a cooling rate of ~0.70 °C/Ma. Then, it underwent slow cooling during 60–38 Ma at a rate of ~0.45 °C/Ma, followed by a final accelerated cooling at rate of ~1.45 °C/Ma since 38 Ma. The thermal histories of sample HJP from the center of *DSA* showed that the first cooling occurred during 108–55 Ma and caused the sample to cool from 125 °C to ~75 °C at a rate of ~0.94 °C/Ma. It cooled slowly at

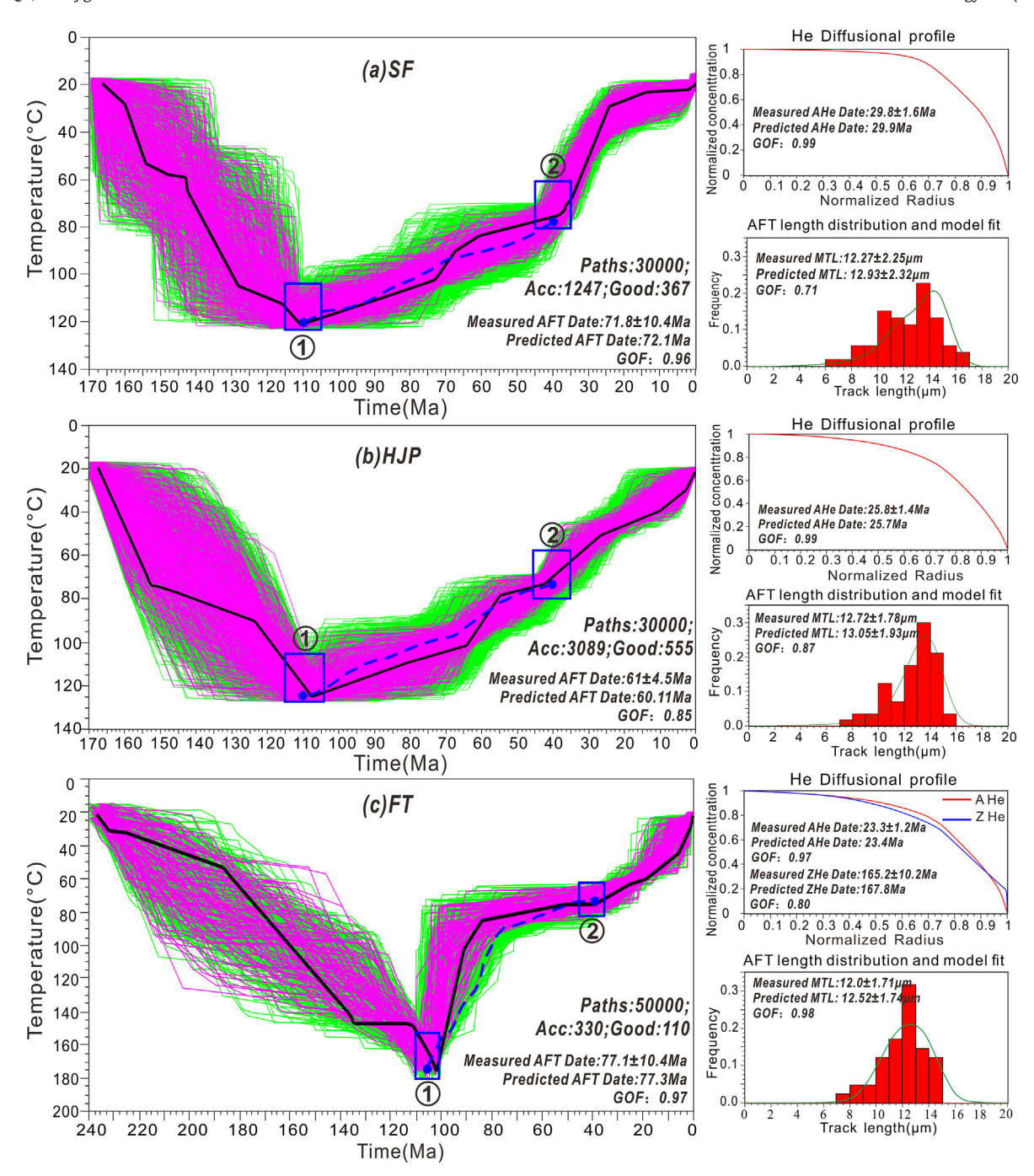


Fig. 8. Thermo-kinematic results reconstructed by AFT, AHe, ZHe and kinematic constrains. Green lines = acceptable fit paths (GOF>0.05), Magenta lines = good fit paths (GOF>0.5), Black lines represent the best time-temperature paths. GOF = goodness of fit. ACC = acceptable. MTL = mean track length. The blue boxes, imposed by the range of temperature sensitivities and kinematic simulation results, represent constraints for the Alpine and Himalayan exhumation event. The blue dash lines represent the temperature-time paths of samples. Thermo-kinematic results suggest the sample FT experienced the first cooling stage at ~100 Ma, while the Sample HJP and SF began to cool rapidly at ~108 Ma and 110 Ma. The initial time of rapid uplift during the Alpine stage was getting later from northwest to southeast, which is consistent with the kinematic evolution of sandbox experiment and DEM simulation. Thermo-kinematic results provide more convergent thermal histories (Fig. 8) and more reasonable tectono-thermal evolution results. (For interpretation of the references to color in this figure legend, the reader is referred to the Web version of this article.)

rate of ~0.45 °C/Ma during 55–43 Ma and experienced accelerated cooling at rate of ~1.16 °C/Ma after 43 Ma. The thermal histories of sample FT from the southeastern of **DSA** showed that the first cooling began at ~100 Ma and continued to 80 Ma. The temperature decreased from ~175 °C to ~70 °C at a cooling rate of ~5.25 °C/Ma. During 80-40 Ma, the sample began to cool rapidly at rate of ~0.25 °C/Ma. After 40 Ma, sample FT experienced the second rapid cooling at a rate of ~1.00 °C/Ma. The thermal histories of three

samples suggested that the initial time of rapid uplift during the early Late Cretaceous was getting later from northwest to southeast, which is consistent with the kinematic evolution of sandbox experiment and DEM simulation.

Ro data and the EASY Ro% model [94] were applied to reconstructed the denudation process in our study. Ro is the most commonly used indicator for organic matter maturity and can reveal the maximum paleotemperature. The EASY Ro% model is

currently the most widely applied method for inverting the maximum paleotemperatures using Ro data. The model proposes that a series of successive sedimentary strata reach their maximum temperatures simultaneously and a paleo-geothermal gradient upon reaching the maximum paleotemperature can be obtained, based on the maximum temperatures of a series of samples (Ro) at different depths. Ro data of DS1, DY5 and DY2 was measured from dark shale cuttings at Wuxi Research Institute of Petroleum Geology (Fig. 9a). The maximum gradients (G) shown as dashed and dotted lines in Fig. 9b are calculated using the maximum paleotemperatures reconstructed by Ro data. The maximum paleotemperature profiles of three wells revealed the maximum paleogeothermal gradient of **DSA** before denudation was approximately 30 °C/km.

The Mesozoic-Cenozoic exhumation history can be restored combining with the paleo-geothermal gradient and the best-fit time-temperature paths. Based on the modeled paleotemperature $(T_p, {}^{\circ}C)$ and paleo-geothermal gradient $(G, {}^{\circ}C/km)$, the exhumation $(\Delta h, m)$ was calculated using the following equation:

$$\Delta h = (T_p - T_0)/G - Z_0 \tag{3}$$

where Z_0 is the present burial depth in m, T_0 is the paleo-surface temperature with 20 °C. The deformation is characterized by a 'rapid-slow-rapid' uplift process, including (1) the first period rapid uplift during the Early Cretaceous—Late Cretaceous, which is consistent with the fast Pacific-Eurasia convergence [82]; (2) a period of slow uplift during the Late Cretaceous-Eocene due to the change in the rate of Pacific-Eurasia convergence [82] and the SEEward retreat of the subducted Pacific slab [44]; (3) the second period rapid uplift after the Eocene because of the India-Asia collision. During the Alpine stage, the uplift time of Well DY2 is ~110 Ma and the denudation is 1550 m, while the Well DY5 began to uplift at 108 Ma with denudation of 3550 m. During the

Himalayan, the denudation of three wells were all ~1800 m. This result indicated that differential uplift of Alpine is the main cause of significant differential erosion in *DSA*.

6. Dynamic evaluation of shale gas preservation and loss

To study dynamic evaluation of shale gas preservation and loss, we first reconstructed the 'burial-hydrocarbon generation-uplift-gas loss' evolution of shale, including the burial history, thermal history, hydrocarbon generation history, pressure evolution and shale gas content evolution. It can dynamically reflect the characteristics of temperature and pressure evolution and quantitatively characterize the changes of shale gas content during differential uplift process. The specific process includes: (1) restored the thermal history and paleo-geothermal gradient history of shale and get accurate denudation; (2) reconstructed the burial history and hydrocarbon generation history based on the tectonic evolution process, thermal history and denudation; (3) restored the pressure evolution; (4) reconstructed the burial-hydrocarbon generation-erosion evolution of shale combining the burial history, thermal history, hydrocarbon generation history and pressure evolution.

6.1. Pressure evolution

The basin simulation method was required to restore the pressure evolution and the pore pressures reconstructed by inclusions simulation. Based on the Ro, erosion and the thermal histories reconstructed, the burial and thermal history of DY1 were reconstructed by the BasinMod 1D (Fig. 10a). According to the method proposed by Zhang and Frantz (1987) [95], the trapping pressures of inclusions were calculated (Table 6):

$$P = A_1 + A_2T \tag{4}$$

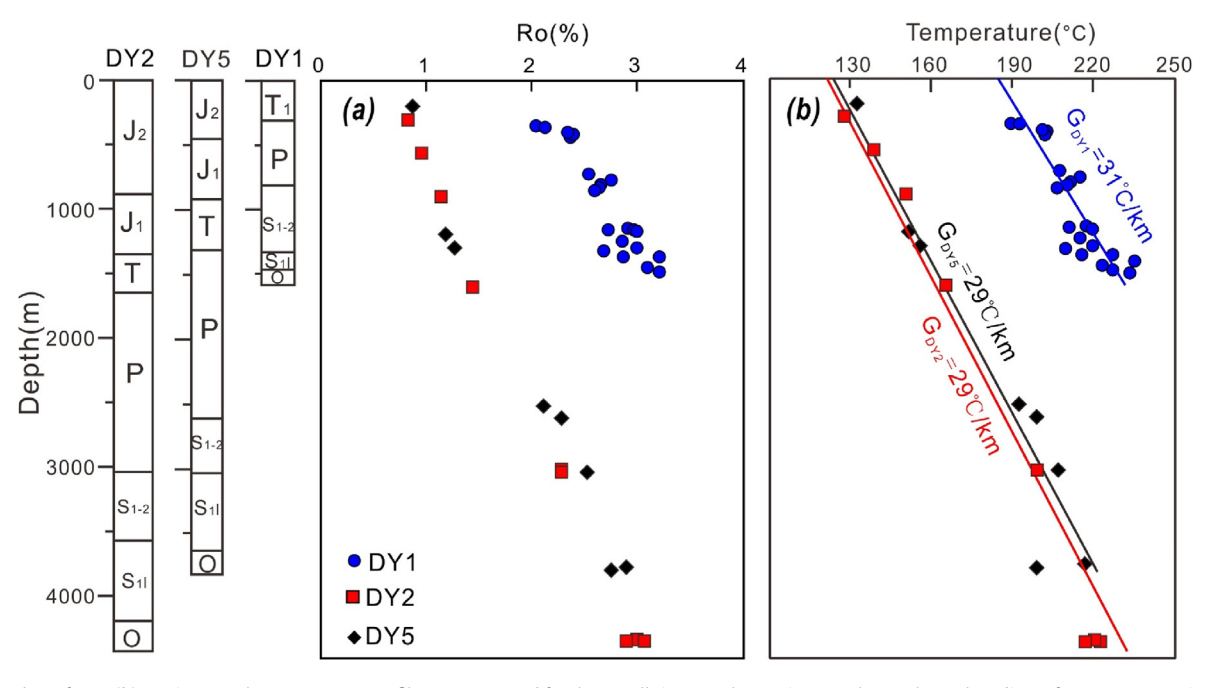


Fig. 9. (a) Ro data of DSA. (b) Maximum paleotemperature profiles reconstructed for three wells in DSA. The maximum paleogeothermal gradient of DSA was approximately 30 °C/km. O: Ordovician. S₁: the lower Silurian Longmaxi Formation. S₁₋₂: the middle-lower Silurian. P: Permian. T: Triassic. J₁: the lower Jurassic. J₂: the middle Jurassic.

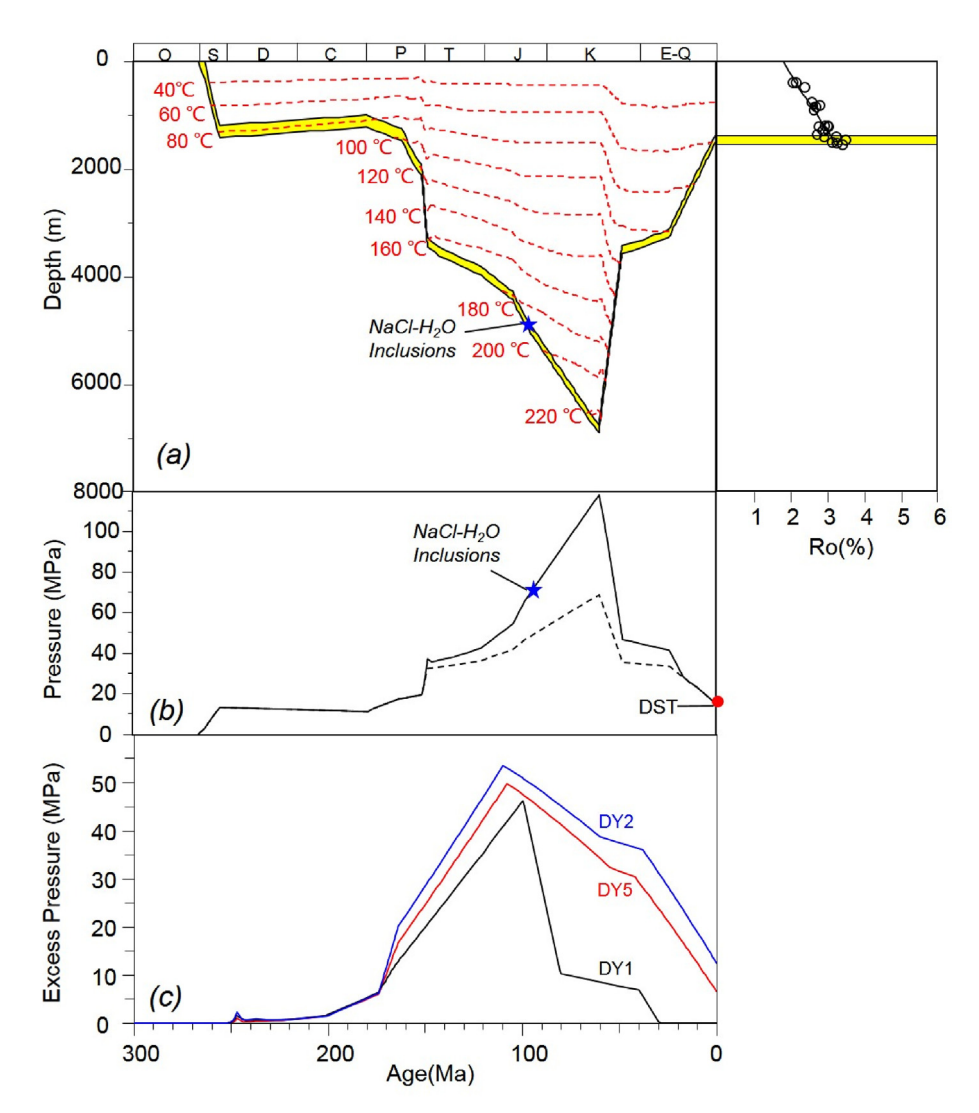


Fig. 10. (a) Burial and thermal history for the lower Silurian Longmaxi Formation of Well DY1. Previous works on the paleo-heat flow in the southeastern Sichuan Basin [97–99] were considered as determinate restraints; The red dashed lines in the left represent the temperature; The circles in the right represent the measured Ro data; The black line in the right represents the simulation values. O: Ordovician. S: Silurian. D: Devonian. C: Carboniferous. P: Permian. T: Triassic. J: Jurassic. K: Cretaceous. E–Q: Paleogene and Neogene. (b) The pressure evolution in the lower Silurian Longmaxi Formation of Well DY1. The stars represent the pressure and time results of NaCl–H₂O inclusions; The filled dots are the drilling measured data (drilling stem test-DST); The black dashed black line represents the hydrostatic pressure. (c) The evolution of excess pressure of the lower Silurian Longmaxi Formation in three wells of DSA. Since the Early Cretaceous, the lower Silurian Longmaxi Formation experienced a 'rapid-slow-rapid' pressure decreasing process. The differential pressure distribution in plane mainly occurred in the Alpine stage. (For interpretation of the references to color in this figure legend, the reader is referred to the Web version of this article.)

 $\begin{tabular}{ll} \textbf{Table 6} \\ \textbf{The inclusions data in quartz and the results of trapping pressure of S_1l.} \\ \end{tabular}$

Sample	Inclusion system	Homogenization temperature ($^{\circ}$ C)	wt%NaCl	Freezing temperature (°C)	Gas/Liquid (%)
DY1	NaCl-H ₂ O	165.1–210.2 185.6 (7) *	3.2	-22.5~-4.8 -14.0 (7)	6.0
Sample	Trapping time (Ma)	Trapping temperature (°C)	Trapping pressure (MPa)	Paleo-depth (m)	Pressure Coefficient
DY1	158	185.6	71.3	4950	1.47

^{*165.1—210.2} represents the range of homogenization temperate, 185.6 represents the average of homogenization temperature, (7) represents the number of samples. The inclusions data were provided by the SINOPEC Exploration Company.

$$A_{1} = 6.100 \times 10^{-3} + \left(2.358 \times 10^{-1} - a_{1}\right) T_{h} - \left(2.855 \times 10^{-3} + a_{2}\right) T_{h}^{2} - \left(a_{3} T_{h} - a_{4} T_{h}^{2}\right) m$$
(5)

$$A_2 = a_1 + a_2 T_h + 9.888 \times 10^{-6} T_h^2 + (a_3 + a_4 T_h) m$$
 (6)

where P is the trapping pressure, MPa; T is the trapping temperature, ${}^{\circ}C$, which equal to the homogenization temperature (Th, ${}^{\circ}C$) in the brine inclusions [96]; a_1 , a_2 , a_3 and a_4 with values of

28.73, -6.477×10^{-3} , -2.009×10^{-1} and 3.186×10^{-3} , are fit parameters of NaC1-H₂0, KC1-H₂0, CaC1₂-H₂0 and H₂0 fluids, respectively; m is the molality, %. At 1956 m, one set of NaCl-H₂O inclusions were measured with the homogeneous temperatures of 185.6 °C. The minimum capture pressure calculated by inclusion simulation was 71.3 MPa. Based on the temperature, the burial depth and geological age could be read from the burial history. which was ~158 Ma at 4950 m. Therefore, the pressure coefficient was 1.47 during the Middle-Late Jurassic, the very period with accumulating overpressure. Corrected by the constrains of inclusions pressures and present pressures, the pressure evolution of the lower Silurian Longmaxi Formation (Fig. 10b) could be simulated under the Bmod Fluid Flow model. The result showed that (1) the overpressure began at the Early Triassic (~250 Ma), which was relatively stable during the Early Jurassic period; (2) at the end of the Jurassic (175 Ma), the overpressure increased rapidly, reaching the maximum at 100 Ma (~110.0 MPa); (3) with the rapid uplift from the Late Cretaceous, the pressure decreased rapidly, even to the normal at the Oligocene (~30 Ma).

Based on the simulation parameters of well DY1, the excess pressure evolutions of other wells were reconstructed (Fig. 10c). The results showed that the overpressure reached the maximum at the Late Cretaceous, while the maximum decreased from northwest to southeast. Affected by the uplift since the Early Cretaceous, the lower Silurian Longmaxi Formation experienced a 'rapid-slow-rapid' pressure decreasing process and the reduction was different in different periods. The pressure of well DY1 decreased faster than other wells during the Alpine stage, while it was opposite during the Himalayan. However, there were less pressure reduction in the well DY2 and DY5 and some overpressures are still retained, with pressure coefficients of 1.55 and 1.30, respectively. This indicated the differential pressure distribution of the lower Silurian Longmaxi Formation in plane mainly occurred in the Alpine stage.

6.2. Dynamic analysis of shale gas preservation

The evolution of temperature and pressure allow us to estimate the shale gas content during the uplift process according to the quantitative calculation method for shale gas occurrence proposed by Yu et al. (2016) [100]. Firstly, the adsorbed gas content was calculated based on the TOC content, temperature and pressure under burial conditions. In addition, free gas storage space was derived by deducting the volume of pore water and adsorbed gas from total space. Then, the density of free gas was calculated using the Peng-Robinson (PR) equation [101]. Finally, the free gas content was calculated (see Supplemental Material S2). Note that the current shale gas content calculated is consistent with actual exploration. Therefore, we believe that this result can be regarded as shale gas content evolution of **DSA**.

Confined by Ro, denudation, temperature, pressure and gas content, we attempt to reconstruct the burial-hydrocarbon generation-erosion evolution of the lower Silurian Longmaxi Formation shale (Fig. 11). The shale experienced the rapid subsidence during the Middle-Late Silurian and continuous uplift from Devonian to Carboniferous. During this period, the shale buried shallow and it was always in the low mature stage. The bottom of the lower Silurian Longmaxi Formation shale entered the hydrocarbon generation threshold (Ro = 0.5%) in the Early Devonian. With the rapid buried, the maturity of shale increased rapidly after the Early Permian. The shale reached the main gas stage (1.3% < Ro < 2.0%) in the Early Triassic and rapidly entered the dry-gas stage (Ro > 2.0%) in the Late Jurassic. The maturity reached the maximum in the Late Cretaceous and the shale gas content, temperature and pressure also reached the maximum. Affected by the differential uplift since the Early Cretaceous, there are obvious differences in the process of temperature and pressure decreased. The shale gas was also characterized by differential loss. The well DY1 is located in the northwestern DSA. During the Early Cretaceous-Eocene (100-40 Ma), the temperature, pressure and shale gas content of the lower Silurian Longmaxi Formation shale decreased from 230 °C, 118 MPa and 6.37 m^3/t to 103 °C, 42 MPa and 4.27 m^3/t as a result of the huge Alpine uplift (~3550 m). The Himalavan uplift since the Eocene caused the temperature, pressure and shale gas content decreasing to 60 °C, 15 MPa and 3.15 m³/t. The well DY5 lies in the center of DSA. From the Early Cretaceous (108 Ma) to the Eocene (43 Ma), the moderate Alpine uplift (~1750 m) resulted in the temperature and pressure decreasing with values of 68 °C and 37 MPa and the shale gas loss was 0.42 m³/t. Since then, the temperature, pressure and shale gas content decreased to the present values of 111 °C, 48 MPa and 6.22 m³/t due to the Himalayan uplift. The well DY2 is located in the southeastern DSA. There was 61 °C, 32 MPa and 0.22 m³/t in the decreasing of the temperature, pressure and shale gas content in response to the moderate Alpine uplift (~1550 m) during the Early Cretaceous-Eocene (110-38 Ma). From the Eocene to the present time, the temperature, pressure and shale gas content decreased to 113 °C, 67 MPa and 7.45 m³/t because of the Himalayan uplift. With a trend of decreasing from southeast to northwest, the shale gas loss of the lower Silurian Longmaxi Formation mainly occurred in the Alpine stage. This suggested that the differential uplift of Alpine resulted in differential distribution of gas content in plane.

7. Discussion

7.1. Thermo-kinematic constraints on the tectono-thermal evolution of fold-and-thrust belts

Kinematic analysis is one of the main fields of structural geology research in fold-and-thrust belts and the methods include sandbox experiment, numerical simulation and thermo-chronology, etc. Sandbox experiments forward simulates the formation process with visual phenomena and is convenient to analyze the structural deformation characteristics and dynamic mechanism. But it cannot reveal the microscopic information during experimental process, such as displacement, temperature, etc. Numerical simulation mainly includes finite element and discrete element method. It is convenient for quantitative research on displacement and stress field, while suitable geological model and mechanical parameters should be set. Thermo-chronology inverse simulates the tectonic evolution by restoring the thermal histories of samples and quantitatively characterize the multi-stage uplift process. Some certain geological constraints, including time and temperature ranges, are required for thermal history reconstructed by thermochronology [102,103]. The temperature range is given based on the temperature sensitivities expected for thermo-chronometers and the time range is estimated by regional tectonic evolution. Different views on the uplift process and dynamics mechanism will inevitably lead to different constraints and different thermal histories. In the southeastern Sichuan Basin, for example, the Mesozoic-Cenozoic uplift process has been intensively investigated by thermochronology. Nevertheless, the thermal paths constrained by the apatite fission track indicate the uplift process remains controversial, while it can be divided into three stages (rapid-slow-rapid) [50,56,93,104], two stages (slow-rapid) [48] or one stage [49,105–107]. Moreover, the thermochronology data indicate the initial uplifting time in the Qiyueshan anticline was quite different, which is about 100 Ma [46,47,105] or 80 Ma [48,56]. In addition, the denudation in the same area was also controversial. For example, the denudation since the Late Cretaceous in the southeastern Sichuan Basin restored by Deng et al. (2013) was about 2500 m [42], which is s far

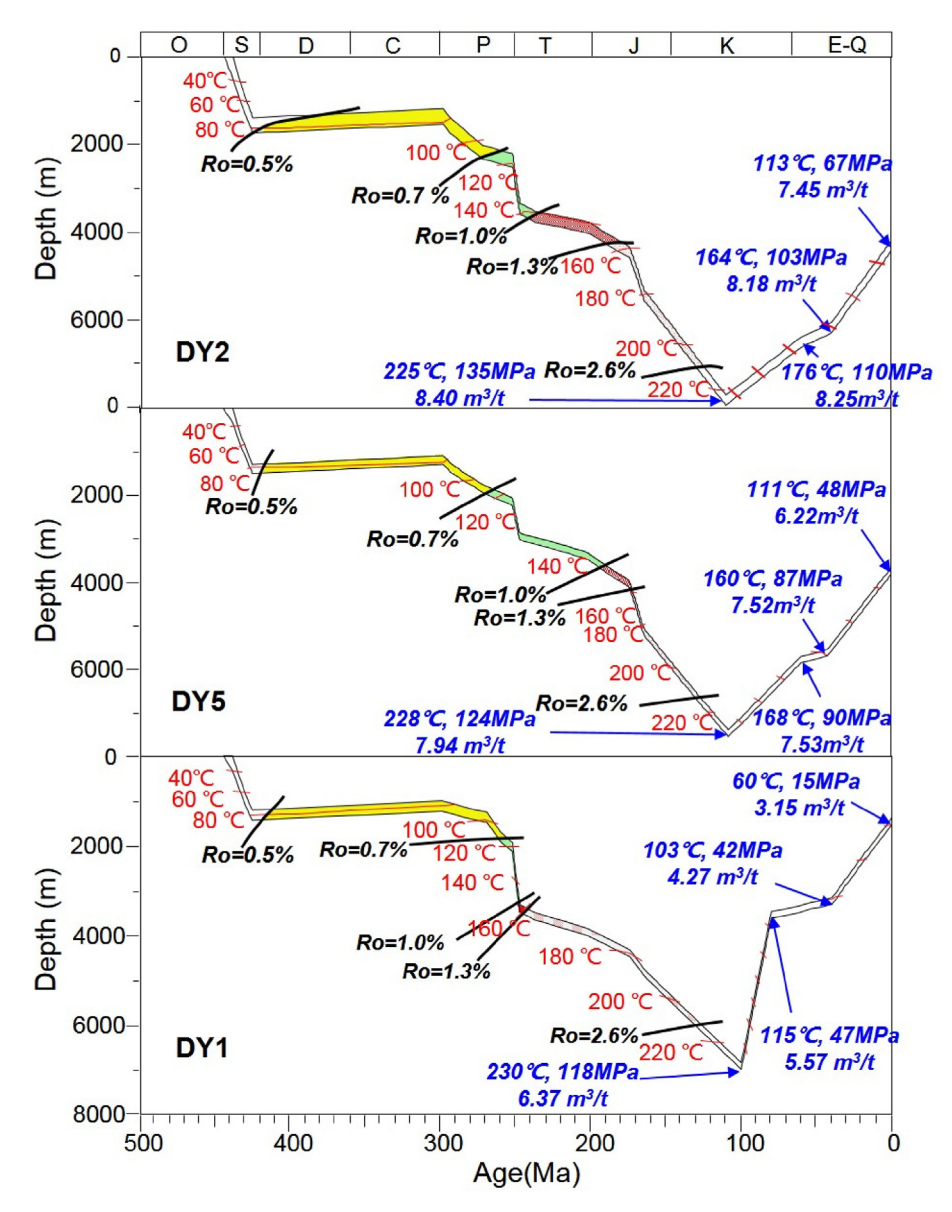


Fig. 11. The 'burial-hydrocarbon generation-uplift-gas loss' evolution of the lower Silurian Longmaxi Formation shale. O: Ordovician. S: Silurian. D: Devonian. C: Carboniferous. P: Permian. T: Triassic. J: Jurassic. K: Cretaceous. E—Q: Paleogene and Neogene. 230 °C, 118.0 MPa represents the temperature and pressure of the bottom of the lower Silurian Longmaxi Formation shale; 6.37 m³/t represents the shale gas content of the bottom of the lower Silurian Longmaxi Formation. Since the Early Cretaceous, there are obvious differences in the process of temperature and pressure decreasing and shale gas losing. The shale gas loss of the lower Silurian Longmaxi Formation mainly occurred in the Alpine stage.

less than the results recovered by other scholars [48,105].

Essentially, thermal histories are often used to reflect the cooling processes of samples during the formation of a fold-and-thrust belt. However, there are obvious differential horizontal displacement (Figs. 6 and 7). The information of the horizontal motion contained in the thermal histories is always overlooked, which has a significant effect on the kinematic analysis for the area with long horizontal displacement. In recent years, some scholars have proposed the thermo-kinematic method to study tectonic evolution of fold-and-thrust belts [108–110]. Almendral et al. (2015) has proposed the FetKin, a C++ program for forward thermo-kinematic modeling, by coupling the balanced reconstruction (2DMove), finite element computation of temperatures and thermochronological ages [108]. This method has achieved satisfactory application results in the study of the structural evolution of the Colombian Eastern Cordillera [68] and the Tajik fold-and-thrust

belt [110]. However, they also overlooked the obvious differential horizontal displacement and the thermal histories may not reveal the thrusting process accurately.

In this study, we demonstrated new insight for kinematic restorations in the thrust nappe with differential horizontal displacement. The deformation process was first identified by sandbox experiments and DEM, Then, some kinematic constraints were given to the thermal modeling. In this process, we have considered the horizontal displacement information. Finally, the uplift process was reconstructed by the best time—temperature path and Ro data. Compared with the thermal histories reconstructed by low-temperature thermochronology data (Fig. 5), thermo-kinematic analysis can provide a more convergent thermal histories (Fig. 8) and more reasonable tectono-thermal evolution results. This method also has limitations: the temperature paths converted by recorded kinematic paths of particles may not match

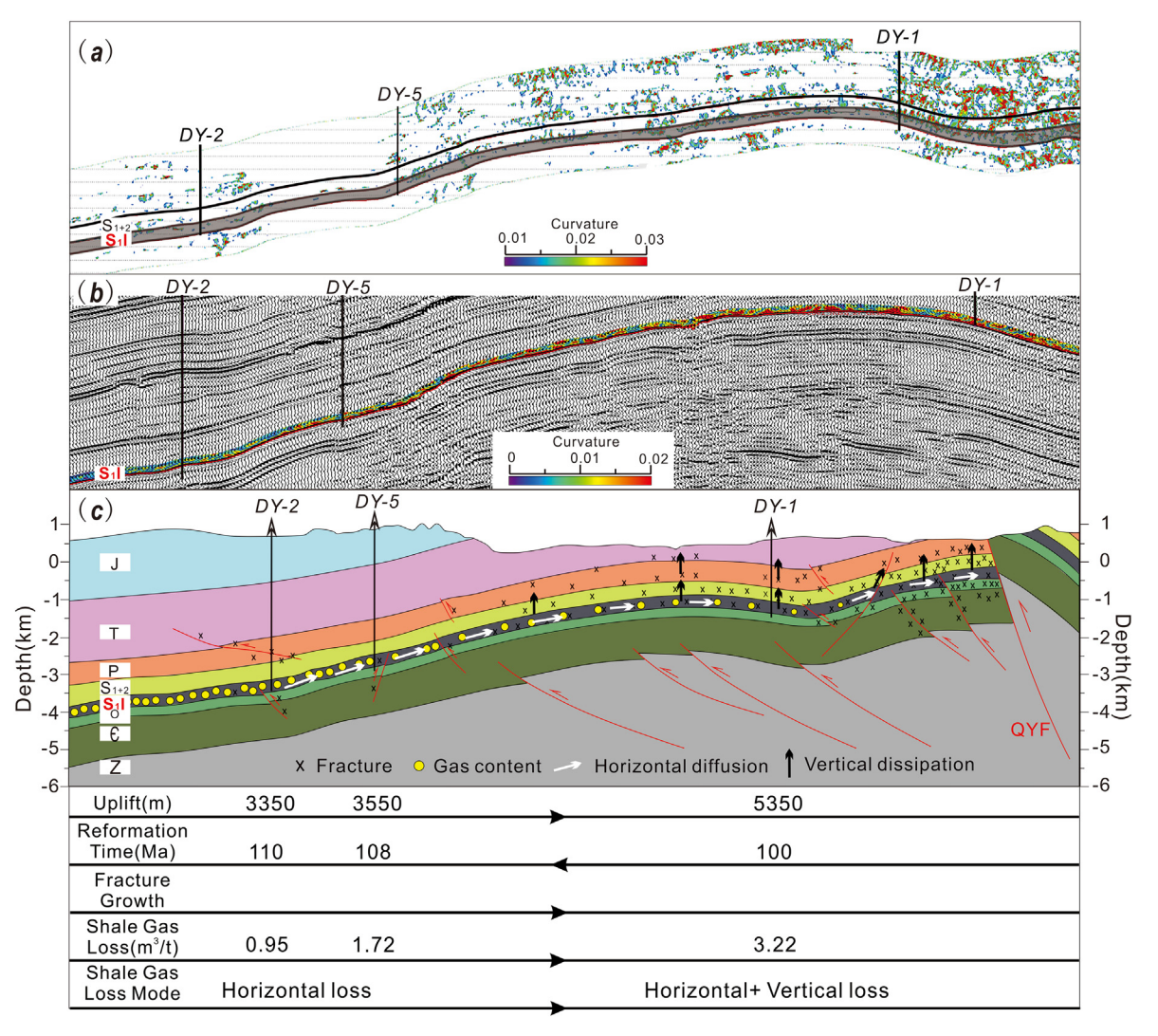


Fig. 12. Influence of differential tectono-thermal evolution on shale gas preservation in *DSA*. (a) The characteristics of fracture growth in roof predicted by the curvature attribute. The roof includes the middle Silurian green silty mudstone and the upper section of the lower Silurian Longmaxi Formation. (b) The characteristics of fracture growth in the lower Silurian Longmaxi Formation shale. (c) the model of shale gas loss in *DSA*. The 'X' represents the fracture growth and few 'X' indicates few fractures. The yellow circles represent the shale gas content and more circles suggest more gas content. From northwest to southeast, the uplift extent, fracture and shale gas loss gradually increased, the reformation time became later, and the loss mode of shale gas gradually changed from lateral diffusion to the coexistence of lateral diffusion and vertical dissipation. (For interpretation of the references to color in this figure legend, the reader is referred to the Web version of this article.)

the thermal histories well. We suggest there are two reasons. (1) Sandbox experiments and DEM can reveal the deformation sequence of fold-and-thrust belts, which indicates we can get accurate initial uplift time of some structures. But they cannot restore the structural uplift amplitude perfectly. Higher amplitude will be generally occurred in DEM; (2) The geothermal gradient plays an important role in the transformation of kinematic path into temperature path. For example, the geothermal gradient in Sichuan Basin has gradually decreased since the Cretaceous [111]. If only the present (or the Cretaceous) geothermal gradient is used to convert kinematic path to temperature path, same uplift amplitude will result in more (or less) temperature reduction. Therefore, the temperature path converted by kinematic path is for thermal evolution reference only and we cannot give accurate constraints in temperature ranges to the thermal modeling. In this study, we only gave the time range based on sandbox experiments and numerical simulations, while the temperature range was also constrained by the sensitivities of ZHe, AFT and AHe ages.

7.2. Influence of differential tectono-thermal evolution on shale gas preservation

Multi-stage tectonic evolution played an important role in the shale gas preservation. For one thing, the thermal evolution of shale is complex due to multi-stage uplift, resulting in multi-stage hydrocarbon generation and expulsion. For another, the energy field (pressure, temperature, stress, fluid chemical, etc.) and the mechanical properties of shale will be changed during uplift process. Compared with carbonate rock and sandstone, shale usually has stronger plasticity and certain survivability for its low porosity and low permeability. However, when late tectonic movement results in intensive uplifting, denudation, folding and faulting, the pressure system is destructed and the caprock losses plasticity, which may cause the sealing and preservation conditions of shale is getting worse. During the uplift process, pre-existing micro fractures in the shale will be re-opened due to pressure relief. In **DSA**, for example, after reaching the maximum burial depth, the microfractures generated by gas expansion resulted from shale uplift and

unloading effectively improved the connectivity of various pores [20,23,24]. In the later uplift process, the horizontal fractures were fused to increase the horizontal permeability, which resulted in lateral diffusion of shale gas. With further uplift, a large number of vertical fractures would form to destroyed the continuity of shale gas interval, overlying caprock, allowed the shale gas to dissipate vertically. Here we build a model of shale gas loss in **DSA** (Fig. 12). In Well DY-2 and Well DY-5, there are a few fractures in the shale and roof and shale gas mainly diffuses laterally. In Well DY-1, the enormous uplift occurred since the Early Cretaceous resulted in obvious fractures in the shale and roof. It caused vertical dissipation and lateral diffusion of shale gas.

Previous studies show that the preservation of shale gas is controlled by the intensity and duration of late tectonic movements [16,18,20,21,37]. The exploration practice has showed that pressure is a comprehensive indicator for sealing condition and the pressure coefficient has a positive correlation with shale gas content [15,21,51]. The pressure coefficient of shale is increased from southeast to northwest, while the pressure coefficient of shale in the basin is more than 2 and the pressure coefficient of shale outside the basin is generally less than 1 (Fig. 1), which indicates the preservation condition of shale gas is getting worse from southeast to northwest. Meanwhile, this area experienced progressive tectonic deformation from southeast to northwest in the period from ~180 Ma to ~80 Ma [40,46-48,50,93,104]. This consistency indicated the reformation time of Alpine-Himalayan tectonic movements has a great impact on the preservation of shale gas. However, our results suggested the reformation time became later from northwest to southeast, while the shale gas diffusion loss decreased from southeast to northwest. This shows that the preservation of shale gas is controlled by the intensity of late tectonic, rather than reformation time. Strong uplift in a short time is destructive to the preservation of shale gas, while moderate uplift in a long time is constructively. The gradual deterioration of shale gas preservation conditions from southeast to northwest in the southeast Sichuan basin and its peripheral regions is mainly caused by different intensity of late tectonic. The characteristics of faults development (Fig. 1) which indicates the intensity of late tectonic in the Hubei-Hunan-Guizhou Fold Belt is much stronger than that of the southeast Sichuan basin.

8. Conclusions

With the high natural gas price and enormous energy demands, shale gas has recently been the focus of energy exploration and has a profound impact on the energy markets. Tectonism significantly affects the shale gas preservation. The influence of tectono-thermal evolution on shale gas preservation was analyzed quantitatively in a case study from **DSA**, South China. As a thrust nappe structure, **DSA** is characterized by significant differential vertical uplift, horizontal zoning of gas content in the lower Silurian Longmaxi Formation shale. Here, the Mesozoic-Cenozoic uplift history was constrained by new thermo-kinematic method combining sandbox experiment, DEM, thermochronology and Ro data. The results indicate that there are differential uplift processes during Alpine-Himalayan. Differential uplift of Alpine resulted in significant differential uplift. The Alpine uplift process shows periodic uplift characterized by early rapid uplift and late slow uplift accompanied with differential horizontal displacement. From southeast to northwest, the uplift time changed from 100 Ma to 110 Ma, while the erosion decreased from 3550 m to 1550 m. During the Himalayan, the uplift process was characterized with a rapid uplift as a whole with a deduction of 1800 m. The Alpine stage is the main stage causing significant differential uplift. We demonstrated that compared with the thermal histories reconstructed by lowtemperature thermochronology data, thermo-kinematic analysis could provide a more convergent thermal histories and more reasonable tectono-thermal evolution results.

The 'burial-hydrocarbon generation-uplift-gas loss' evolution of the lower Silurian Longmaxi Formation shale was reconstructed based on the burial history, thermal history, hydrocarbon generation history, pressure evolution and shale gas content evolution. It can dynamically reveal the characteristics of temperature and pressure evolution and quantitatively characterize the changes of shale gas content during differential uplift process. The results show that the buried depth, maturity, temperature, pressure and shale gas content of the shale reached the maximum in the Late Cretaceous. Affected by the differential uplift since the Early Cretaceous, the lower Silurian Longmaxi Formation shale experienced a 'rapid-slow-rapid' differential cooling and pressure decreasing process and there were obvious differences in the shale gas diffusion losing, which mainly occurred in the Alpine stage. The shale gas loss mode suggests the preservation of shale gas is controlled by differential uplift and erosion. With moderate uplift, there are few fractures in the shale and roof and shale gas mainly diffuses laterally, while enormous uplift resulted in obvious fractures and lateral diffusion and vertical dissipation.

Credit author statement

Qianqian Feng: Formal analysis, Investigation, Methodology, Visualization, Writing - original draft. Nansheng Qiu: Conceptualization, Funding acquisition, Project administration, Supervision, Writing - review & editing. Tenger Borjigin: Investigation, Funding acquisition, Project administration Resources, Writing - review & editing. Hang Wu: Formal analysis, Investigation, Methodology, Writing - review & editing. Jiatang Zhang: Formal analysis, Writing - review & editing. Baojian Shen: Resources, Writing - review & editing. Jiangshan Wang: Investigation, Methodology, Writing - review & editing.

Declaration of competing interest

The authors declare that they have no known competing financial interests or personal relationships that could have appeared to influence the work reported in this paper.

Acknowledgments

The National Natural Science Foundation of China (No. 41830424, U19B6003, 41690133) and the National Key R&D Program of China (No. 2017YFC0603102) provided financial support. We gratefully acknowledge the SINOPEC Exploration Company and the Wuxi Research Institute of Petroleum Geology for providing geologic information and core samples. Prof. Zhina Liu gave helpful suggestions and provided the PFC2D software. All of the data used for this study are contained within the manuscript and supplementary material.

Appendix A. Supplementary data

Supplementary data to this article can be found online at https://doi.org/10.1016/j.energy.2021.122781.

References

- [1] Guo MY, Xu Y, David Chen YQ. Catching environmental noncompliance in shale gas development in China and the United States. Resour Conserv Recycl 2017;121:73—81.
- [2] Li YB, Li Y, Wang BQ, Chen ZE, Nie D. The status quo review and suggested policies for shale gas development in China. Renew Sustain Energy Rev

- 2016;59:420-8.
- [3] Yang HJ, Han X, Wang L. Is there a bubble in the shale gas market? Energy 2021;215:119101.
- [4] Caporin M, Fontini F. The long-run oil—natural gas price relationship and the shale gas revolution. Energy Econ 2017;64:511—9.
- [5] Nick S, Thoenes S. What drives natural gas prices? a structural VAR approach. Energy Econ 2014;45:517—27.
- [6] The U.S. Energy Information Administration (EIA), How much shale gas is produced in the United States? Available at: https://www.eia.gov/tools/faqs/ faq.php?id¼907& t¼8. [Accessed 4 March 2020].
- [7] Wang Q, Zhan LN. Assessing the sustainability of the shale gas industry by combining DPSIRM model and Raga-PP techniques: an empirical analysis of Sichuan and Chongqing, China. Energy 2019;176:353—64.
 [8] Ma XH, Wang HY, Zhou SW, Shi ZS, Zhang LF. Deep shale gas in China:
- [8] Ma XH, Wang HY, Zhou SW, Shi ZS, Zhang LF. Deep shale gas in China: geological characteristics and development strategies. Energy Rep 2021;7: 1903–14
- [9] Slatt RM, O'Brien NR. Pore types in the Barnett and Woodford gas shales: contribution to understanding gas storage and migration pathways in finegrained rocks. AAPG (Am Assoc Pet Geol) Bull 2011;95:2017–30.
- [10] Gou QY, Xu S, Hao F, Yang F, Zhang BQ, Shu Z, Zhang AH, Wang YX, Lu YB, Cheng X, Qing JW, Gao MT. Full-scale pores and micro-fractures characterization using FE-SEM, gas adsorption, nano-CT and micro-CT: a case study of the Silurian Longmaxi Formation shale in the Fuling area, Sichuan Basin, China. Fuel 2019;253:167-79.
- [11] Ferrill DA, McGinnis RN, Morris AP, Smart KJ, Sickman ZT, Bentz M, Lehrmann D, Evans MA. Control of mechanical stratigraphy on bed-restricted jointing and normal faulting: Eagle Ford Formation, south-central Texas. AAPG (Am Assoc Pet Geol) Bull 2014;98:2477–506.
- [12] Curtis JB. Fractured shale-gas systems. AAPG (Am Assoc Pet Geol) Bull 2002;11:1921–38.
- [13] Julia FWG, Stephen EL, Jon EO, Peter E, Fall A. Natural Fractures in shale: a review and new observations. AAPG (Am Assoc Pet Geol) Bull 2014;98: 2165–216.
- [14] Zhu HJ, Ju YW, Huang C, Chen FW, Chen BZ, Yu K. Microcosmic gas adsorption mechanism on clay-organic nanocomposites in a marine shale. Energy 2020:197:117256.
- [15] Guo TL, Zeng P. The structural and preservation conditions for shale gas enrichment and high productivity in the Wufeng-Longmaxi Formation, Southeastern Sichuan Basin. Energy Explor Exploit 2015;33:259–76.
- [16] Guo XS, Hu DF, Li YP, Wei ZH, Wei XF, Liu ZJ. Geological factors controlling shale gas enrichment and high production in Fuling shale gas field. Petrol Explor Dev 2017;44:513–23.
- [17] Ma YS, Cai XY, Zhao PR. China's shale gas exploration and development: understanding and practice. Petrol Explor Dev 2018;45:589–603.
- [18] Li SJ, Li YQ, He ZL, Chen K, Zhou Y, Yan DT. Differential deformation on two sides of Qiyueshan Fault along the eastern margin of Sichuan Basin, China, and its influence on shale gas preservation. Mar Petrol Geol 2020;121: 104602
- [19] Shu Y, Lu YC, Chen L, Wang C, Zhang BQ. Factors influencing shale gas accumulation in the lower Silurian Longmaxi formation between the north and South Jiaoshiba area, Southeast Sichuan Basin, China. Mar Petrol Geol 2020;111:905–17.
- [20] He ZL, Nie HK, Li SJ, Luo J, Wang H, Zhang GR. Differential enrichment of shale gas in upper Ordovician and lower Silurian controlled by the plate tectonics of the Middle-Upper Yangtze, south China. Mar Petrol Geol 2020;118:104357.
- [21] Wei XF, Li YP, Wei ZH, Liu RB, Yu GC, Wang QB. Effects of preservation conditions on enrichment and high yield of shale gas in Sichuan Basin and its periphery. Petrol Geol Exp (Chin) 2017;39:147–53.
- [22] Schloemer S, Krooss BM. Molecular transport of methane, ethane and nitrogen and the influence of diffusion on the chemical and isotopic composition of natural gas accumulations. Geofluids 2004;1:81–108.
- [23] Liu R, Hao F, Engelder T, Zhu ZG, Yi JZ, Xu S, Teng CY. Influence of tectonic exhumation on porosity of Wufeng-Longmaxi shale in the Fuling gas field of the eastern Sichuan Basin, China. AAPG (Am Assoc Pet Geol) Bull 2020;104: 939—59
- [24] Chen Q, Zhang J, Tang X, Li W, Li Z. Relationship between pore type and pore size of marine shale: an example from the Sinian-Cambrian formation, upper Yangtze region, South China. Int J Coal Geol 2016;158:13—28.
- [25] Smart KJ, Öfoegbu GI, Morris AP, McGinnis RN, Ferrill DA. Geomechanical modeling of hydraulic fracturing: why mechanical stratigraphy, stress state, and pre-existing structure matter. AAPG (Am Assoc Pet Geol) Bull 2014;98: 2237–61
- [26] Assad G, Ralf L, Garri G, Christoph H. Assessment of unconventional shale gas potential of organic-rich Mississippian and Lower Pennsylvanian sediments in western Germany. Int J Coal Geol 2018;198:29–47.
- [27] Evans MA, DeLisle A, Leo J, Lafonte CJ. Deformation conditions for fracturing in the middle devonian sequence of the central appalachians during the late paleozoic alleghenian orogeny. AAPG (Am Assoc Pet Geol) Bull 2014;98: 2263-200
- [28] Wilkins S, Mount V, Mahon K, Perry A, Koenig J. Characterization and development of subsurface fractures observed in the Marcellus Formation, Appalachian Plateau, north-central Pennsylvania. AAPG (Am Assoc Pet Geol) Bull 2014;98:2301–45.
- [29] Ferrill DA, Morris AP, Hennings PH, Haddad DE. Faulting and fracturing in

shale and self-source reservoirs: Introduction. AAPG (Am Assoc Pet Geol) Bull 2014;98:2161–4.

- [30] He ZL, Li SJ, Nie HK, Yuan YS, Wang H. The shale gas "sweet window": "The cracked and unbroken" state of shale and its depth range. Mar Petrol Geol 2019;101:334–42.
- [31] Gou QY, Xu S, Hao F, Yang F, Shu ZG, Liu R. The effect of tectonic deformation and preservation condition on the shale pore structure using adsorptionbased textural quantification and 3D image observation. Energy 2021;219: 119579
- [32] Nygård R, Gutierrez M, Bratli RK, Høeg K. Brittle-ductile transition, shear failure and leakage in shales and mudrocks. Mar Petrol Geol 2006;23: 201–12
- [33] Ougier-Simonin A, Renard F, Boehm C, Vidal-Gilbert S. Microfracturing and microporosity in shales. Earth Sci Rev 2016:162:198–226.
- [34] Ju YW, Sun Y, Tan JQ, Bu HL, Han K, Li XS, Fang LZ. The composition, pore structure characterization and deformation mechanism of coal-bearing shales from tectonically altered coalfields in eastern China. Fuel 2018;234: 626–42.
- [35] Ding WL, Dai P, Zhu DW, Zhang YQ, He JH, Li A, Wang RY. Fractures in continental shale reservoirs: a case study of the Upper Triassic strata in the SE Ordos Basin, Central China. Geol Mag 2016;153:663–80.
- [36] Ge X, Hu W, Ma Y, Li M, Tang J, Zhao P. Quantitative evaluation of geological conditions for shale gas preservation based on vertical and lateral constraints in the Songkan area, Northern Guizhou, southern China. Mar Petrol Geol 2021;124:104787.
- [37] Jiang ZX, Song Y, Tsng XL, Li Z, Wang XM, Wang GZ, Xxu ZX, Li X, Zhang K, Chang JQ, Qiu HY. Controlling factors of marine shale gas differential enrichment in southern China. Petrol Explor Dev 2020;47:661–73.
- [38] Liu WP, Wu J, Jiang H, Zhou Z, Luo C, Wu W, Li XJ, Liu SG, Deng B. Cenozoic exhumation and shale-gas enrichment of the Wufeng-Longmaxi formation in the southern Sichuan basin, western China. Mar Petrol Geol 2021;125: 104865.
- [39] Ougier-Simonin A, Renard F, Boehm C, Vidal-Gilbert S. Microfracturing and microporosity in shales. Earth Sci Rev 2016;162:198–226.
- [40] Yan DP, Zhou MF, Song HL, Wang XW, Malpas J. Origin and tectonic significance of a mesozoic multi-layer over-thrust system within the Yangtze block (south China). Tectonophysics 2003;361:239–54.
- [41] Yong T, Fan Y, Lv QQ, Tang WJ, Wang HK. Analysis of the tectonic stress field of SE sichuan and its impact on the preservation of shale gas in lower silurian Longmaxi Formation of the dingshan region, China. J Geol Soc India 2018;92: 92–100.
- [42] Deng B, Liu S, Li Z, Jansa LF, Liu S, Wang G, Sun W. Differential exhumation at eastern margin of the Tibetan Plateau, from apatite fission-track thermochronology. Tectonophysics 2013;591:98–115.
- [43] Liu SG, Deng B, Li ZW, Jansa LB, Liu S, Wang GZ, Sun W. Geological evolution of the longmenshan intracontinental composite orogen and the eastern margin of the Tibetan Plateau. J Earth Sci 2013;24:874–90.
- [44] Li JH, Zhang YQ, Dong SW, Johnston ST. Cretaceous tectonic evolution of South China: a preliminary synthesis. Earth Sci Rev 2014;134:98–136.
- [45] Wang E, Meng K, Su Z, Meng QR, Chu JJ, Chen ZL, Wang G, Shi XH, Liang XQ. Block rotation: tectonic response of the Sichuan basin to the southeastward growth of the Tibetan Plateau along the Xianshuihe-Xiaojiang fault. Tectonics 2014;33:686–718.
- [46] Richardson NJ, Densmore AL, Seward D, Fowler A, Wipf M, Ellis MA, Yong L, Zhang Y. Extraordinary denudation in the Sichuan Basin: insights from lowtemperature thermochronology adjacent to the eastern margin of the Tibetan Plateau. J Geophys Res Solid Earth 2008;113. B04409-n/a.
- [47] Mei LF, Liu ZX, Tang JG, Shen CB, Fan YF. Mesozoic intra-continental progressive deformation in western Hunan-Hubei-eastern Sichuan provinces of China: evidence from apatite fission track and balanced cross-section. Earth Sci (Chin) 2010;35:161–74.
- [48] Li XM, Shan YH. Diverse exhumation of the Mesozoic tectonic belt within the Yangtze Plate, China, determined by apatite fission-track thermochronology. Geosci | 2011;15:349-57.
- [49] Tian YT, Qiu NS, Kohn BP, Zhu CQ, Hu SB, Gleadow AJW, McInnes BIA. Detrital zircon (U-Th)/He thermochronometry of the mesozoic daba Shan foreland basin, central China: evidence for timing of post-orogenic denudation. Tectonophysics 2012;570–571:65–77.
- [50] Wu H, Qiu N, Feng Q, Chang J, Jiang K, Zhang Y, Wu S. Reconstruction of tectonic uplift process with thermo-kinematic method. Chinese. J Geophys 2020:63:2329–44.
- [51] Ma YS, Guo XH, Guo TO, Huang R, Cai XY, Li GX. The Puguang gas field: new giant discovery in the mature Sichuan Basin, southwest China. AAPG (Am Assoc Pet Geol) Bull 2007;91:627–43.
- [52] Liu YF, Qiu NS, Xie ZY, Yao QY, Zhu CQ. Overpressure compartments in the central paleo-uplift, Sichuan Basin, southwest China. AAPG (Am Assoc Pet Geol) Bull 2016;100:867–88.
- [53] Jiang GZ, Hu SB, Shi YZ, Zhang C, Wang ZT, Hu D. Terrestrial heat flow of continental China: updated dataset and tectonic implications. Tectonophysics 2019;753:36–48.
- [54] Li CX, He DF, Sun YP, He JY, Jiang ZX. Structural characteristic and origin of intra-continental fold belt in the eastern Sichuan basin, South China Block. J Asian Earth Sci 2015;111:206–21.
- [55] Wang Y, Qiu NS, Borjigin T, Shen BJ, Xie XM, Ma ZL, Lu CJ, Yang YF, Yang L, Cheng LJ, Fang GJ, Cui Y. Integrated assessment of thermal maturity of the

- upper ordovician-lower silurian wufeng-longmaxi shale in Sichuan basin, China, Mar Petrol Geol 2019;100:447–65.
- [56] Liu SG, Sun W, Li ZW, Deng B, Liu S. Tectonic uplifting and gas pool formation since late cretaceous epoch, Sichuan basin. Nat Gas Geosci 2008:293–300 (in Chinese).
- [57] Green PF, Duddy IR, Gleadow AJW, Tingate PR, Laslett GM. Thermal annealing of fission tracks in apatite: 1. A qualitative description. Chem Geol 1986;59:237–53.
- [58] Gleadow AJW, Duddy IR, Green PF, Hegarty KA. Fission track lengths in the apatite annealing zone and the interpretation of mixed ages. Earth Planet Sci Lett 1986:78:245–54.
- [59] Ketcham RA, Carter A, Donelick RA, Barbarand J, Hurford AJ. Improved modeling of fission-track annealing in apatite. Am Mineral 2007;92: 799–810
- [60] Fitzgerald PG, Malusà MG. Concept of the exhumed partial annealing (retention) zone and age-elevation profiles in thermochronology. Springer Textbooks in Earth Sciences, Geography and Environment; 2019. p. 165–89.
- [61] Wolf RA, Farley KA, Kass DM. Modeling of the temperature sensitivity of the apatite (U-Th)/He thermochronometer. Chem Geol 1998;1–2:105–14.
 [62] Flowers RM, Shuster DL, Wernicke BP, Farley KA. Radiation damage control
- [62] Flowers RM, Shuster DL, Wernicke BP, Farley KA. Radiation damage control on apatite (U-Th)/He dates from the Grand Canyon region, Colorado Plateau. Geology 2007;35:447.
- [63] Farley KA, Shuster DL, Ketcham RA. U and Th zonation in apatite observed by laser ablation ICPMS, and implications for the (U-Th)/He system. Geochem Cosmochim Acta 2011;75:4515–30.
- [64] Reiners PW. Zircon (U-Th)/He thermochronometry. Rev Mineral Geochem 2005;58:151–79.
- [65] Guenthner WR, Reiners PW, Ketcham RA, Nasdala L, Giester G. Helium diffusion in natural zircon: radiation damage, anisotropy, and the interpretation of zircon (U-Th)/He thermochronology. Am J Sci 2013;313:145–98.
- [66] Chang J, Qiu N, Liu S, Cai C, Xu Q, Liu N. Post-Triassic multiple exhumation of the Taihang Mountains revealed via low-T thermochronology: implications for the paleo-geomorphologic reconstruction of the North China Craton. Gondwana Res 2019;68:34–49.
- [67] Galbraith RF. On statistical models for fission track counts. Math Geol 1981:6:471–8.
- [68] Dunkl I. Trackkey: a Windows program for calculation and graphical presentation offission track data. Comput Geosci 2002;1:3–12.
- [69] Donelick RA, O'Sullivan PB, Ketcham RA. Apatite fission-track analysis. Rev Mineral Geochem 2005;58:49–94.
- [70] Farley KA. (U-Th)/He dating: techniques, calibrations, and applications. Rev Mineral Geochem 2002;47:819—44.
- [71] Farley KA, Wolf RA, Silver LT. The effects of long alpha-stopping distances on (U-Th)/He ages. Geochem Cosmochim Acta 1996;60:4223–9.
- [72] Green PF, Crowhurst PV, Duddy IR, Japsen P, Holford SP. Conflicting (U-Th)/ He and fission track ages in apatite: enhanced He retention, not anomalous annealing behavior. Earth Planet Sci Lett 2006;250:407–27.
- [73] Shuster DL, Flowers RM, Farley KA. The influence of natural radiation damage on helium diffusion kinetics in apatite. Earth Planet Sci Lett 2006;249: 149. 61
- [74] Flowers RM, Ketcham RA, Shuster DL, Farley KA. Apatite (U-Th)/He thermochronometry using a radiation damage accumulation and annealing model. Geochem Cosmochim Acta 2009;73:2347—65.
- [75] Ault AK, Flowers RM. Is apatite U-Th zonation information necessary for accurate interpretation of apatite (U-Th)/He thermochronometry data? Geochem Cosmochim Acta 2012;79:60-78.
- [76] Reiners PW, Farley KA. Infuence of crystal size on apatite (U-Th)/He thermochronology: an example from the Bighorn Mountains, Wyoming. Earth Planet Sci Lett 2001:413–20.
- [77] Vermeesch P, Seward D, Latkoczy C, Wipf M, Günther D, Baur H. α-Emitting mineral inclusions in apatite, their effect on (U-Th)/He ages, and how to reduce it. Geochem Cosmochim Acta 2007;71:1737–46.
- [78] Fitzgerald PG, Baldwin SL, Webb LE, O'Sullivan PB. Interpretation of (U-Th)/ He single grain ages from slowly cooled crustal terranes: a case study from the Transantarctic Mountains of southern Victoria Land. Chem Geol 2006;225:91–120.
- [79] Spiegel C, Kohn B, Belton D, Berner Z, Gleadow A. Apatite (U-Th-Sm)/He thermochronology of rapidly cooled samples: the effect of He implantation. Earth Planet Sci Lett 2009;285:105–14.
- [80] Brown RW, Beucher R, Roper S, Persano C, Stuart F, Fitzgerald P. Natural age dispersion arising from the analysis of broken crystals. Part I: theoretical basis and implications for the apatite (U-Th)/He thermochronometer. Geochem Cosmochim Acta 2013;122:478–97.
- [81] He WG, Zhou JX, Yuan K. Deformation evolution of Eastern Sichuan-Xuefeng fold-thrust belt in South China: insights from analogue modelling. J Struct Geol 2018;109:74–85.
- [82] Northrup CJ, Royden LH, Burchfiel BC. Motion of the Pacific plate relative to Eurasia and its potential relation to Cenozoic extension along the eastern margin of Eurasia. Geology 1995;23:719.
- [83] Ding DK, Guo TL, Hu MX, Liu YL. Basement decoupling structure in jiannan-xuefeng-series 1 of the southern structure studies. Petrol Geol Exp 2007;2: 120–32 (in Chinese).
- [84] Zhang XQ, Shan YH, Nie GJ, Ni YJ. Numerical modeling of the Mesozoic east Sichuan fold belt: influence of detachment depth on the fold pattern in the

platform cover. Geotect Metallogenia 2013:622-32 (in Chinese).

- [85] Dong SW, Zhang YQ, Gao R, Su JB, Liu M, Li JH. A possible buried Paleoproterozoic collisional orogen beneath central South China: evidence from seismic-reflection profiling, Precambrian Res 2015;264:1–10.
- [86] Zhang XQ, Shan YH, Ni YJ, Tan ZJ. Numerical modeling of the Mesozoic east Sichuan fold belt: a two-stage tectonic model. Geotect Metallogenia 2015: 1022—32 (in Chinese).
- [87] Liu SG, Ma WX, Luba J, Huang WM, Zeng XL, Zhang CJ. Characteristics of the shale gas reservoir in the lower silurian formation, east Sichuan basin, China. Acta Petrol Sin 2011;27:2239–52.
- [88] Warsitzka M, Kley J, Kukowski N. Salt diapirism driven by differential loading-Some insights from analogue modelling. Tectonophysics 2013;591: 83–97
- [89] Massoli D, Koyi HA, Barchi MR. Structural evolution of a fold and thrust belt generated by multiple décollements: analogue models and natural examples from the Northern Apennines (Italy). I Struct Geol 2006;28:185—99.
- [90] Konstantinovskaya EA, Rodriguez D, Kirkwood D, Harris LB, Theriault R. Effects of basement structure, sedimentation and erosion on thrust wedge geometry: an example from the quebec appalachians and analogue models. Bull Can Petrol Geol 2009;57:34–62.
- [91] Li SJ, Xiao KH, Wang XW, Zhang RQ, Wo YJ, Zhou Y, Cai LG. Thermochronology of detrital minerals in the silurian strata from southern China and its geological implications. Acta Geol Sin 2008:1068–76 (in Chinese).
- [92] Shi HC, Shi XB, Yang XQ, Jiang HY, Long YK. Exhumation process of fangdoushan-shizhu fold belt in meso-neozoic and its tectonic significance in western hubei-eastern chongqing. Prog Geophys 2011;26:1993—2002.
- [93] Shi HC, Shi XB, Glasmacher UA, Yang XQ, Stockli DF. The evolution of eastern Sichuan basin, Yangtze block since Cretaceous: constraints from low temperature thermochronology. J Asian Earth Sci 2016;116:208–21.
- [94] Sweeney JJ, Burnham AK. Evaluation of a simple model of vitrinite reflectance based on chemical kinetics. AAPG (Am Assoc Pet Geol) Bull 1990: 1559–70
- [95] Zhang YG, Frantz JD. Determination of the homogenization temperatures and densities of supercritical fluids in the system NaCl-KCl-CaCl2-H2O using synthetic fluid inclusions. Chem Geol 1987;3:335-50.
- [96] Robert H, Goldstein T, James R. Systematics of fluid inclusions in diagenetic minerals. Society for Sedimentary Geology; 1994.
- [97] Qiu NS, Liu W, Fu XD, Li WZ, Xu QC, Qing ZC. Maturity evolution of lower cambrian qiongzhusi Formation shale of the Sichuan basin. Mar Petrol Geol 2021:128:105061.
- [98] Jiang Q, Qiu N, Zhu C. Heat flow study of the Emeishan large igneous province region: implications for the geodynamics of the Emeishan mantle plume. Tectonophysics 2018;724–725:11–27.
- [99] He LJ, Xu HH, Wang JY. Thermal evolution and dynamic mechanism of the Sichuan basin during the early permian-middle triassic. Sci China Earth Sci 2011:54:1948–54.
- [100] Yu LJ, Fan M, Borjigin T, Liu YX. Shale gas occurrence under burial conditions. Petrol Geol Exp (Chin) 2016;38. 438-444,452.
- [101] Peng DY, Robinson DB. A new two-constant equation of state. Ind Eng Chem Res 1976;1:59–64.
- [102] Johnson JE, Flowers RM, Baird GB, Mahan KH. "Inverted" zircon and apatite (U-Th)/He dates from the Front Range, Colorado: high-damage zircon as a low-temperature (<50°C)thermochronometer. Earth Planet Sci Lett 2017;466:80–90.
- [103] Clinkscales C, Kapp P, Wang H. Exhumation history of the north-central Shanxi Rift, North China, revealed by low-temperature thermochronology. Earth Planet Sci Lett 2020;536:116146.
- [104] Shen CB, Mei LF, Xu SH. Fission track dating of mesozoic sandstones and its tectonic significance in the Eastern Sichuan Basin, China. Radiat Meas 2009;44:945–9.
- [105] Zhu CQ, Qiu NS, Liu YF, Xiao Y, Hu SB. Constraining the denudation process in the eastern Sichuan Basin, China using low-temperature thermochronology and vitrinite reflectance data. Geol J 2019;54:426–37.
- [106] Cao HY, Zhu CQ, Qiu NS. Maximum paleotemperature of main paleozoic argillutite in the eastern Sichuan basin. Chin J Geophys 2016;59:1017–29.
- [107] Wang P, Liu SF, Hao TJ, Wang K. Cretaceous transportation of Eastern Sichuan arcuate fold belt in three dimensions: insights from AFT analysis. Chin J Geophys 2012;55:1662-73.
- [108] Almendral A, Robles W, Parra M, Mora A, Ketcham R, Raghib M. FetKin: coupling kinematic restorations and temperature to predict thrusting, exhumation histories, and thermochronometric ages. AAPG (Am Assoc Pet Geol) Bull 2015;99:1557–73.
- [109] Mora A, Casallas W, Ketcham RA, Gomez D, Parra M, Namson J, Stocklie D, Almendral A, Robles W, Ghorbal B. Kinematic restoration of contractional basement structures using thermokinematic models: a key tool for petroleum system modeling. AAPG (Am Assoc Pet Geol) Bull 2015;99:1575–98.
- [110] Chapman JB, Carrapa B, Ballato P, DeCelles PG, Worthington J, Oimahmadov I, Gadoev M, Ketcham R. Intracontinental subduction beneath the Pamir Mountains: constraints from thermokinematic modeling of shortening in the Tajik fold-and-thrust belt. Geol Soc Am Bull 2017;129(11–12):1450–71.
- [111] Zhu CQ, Hu S, Qiu NS, Rao S, Yuan YS. Thermal history of the Sichuan basin, SW China: evidence from deep boreholes. Sci China Earth Sci 2016;59: 70–82.